geosciences

MDPI

Article

Convective Instability in Intraplate Oceanic Mantle Caused by Amphibolite-Derived Garnet-Pyroxenites—A Xenolith Perspective (Hyblean Plateau, Sicily)

Vittorio Scribano * and Serafina Carbone

Department of Biological, Geological and Environmental Sciences, University of Catania, Corso Italia 57, 95129 Catania, Italy; carbone@unict.it

* Correspondence: scribano@unict.it

Received: 30 June 2020; Accepted: 17 September 2020; Published: 22 September 2020

Abstract: Geochemical characteristics of middle ocean ridge basalts (MORBs) testify partial melting of spinel-peridotite mixed with a few amounts of garnet-pyroxenite. The latter can be considered either autochthonous products of the crystallization of partial melts in the sub-oceanic mantle or allocthonous recycled crustal materials originated in subduction contexts. Here we suggest the "autocthnous recycled" origin for garnet-pyroxenites. Such a hypothesis derives from the study of garnet-bearing pyroxenite xenoliths from the Hyblean Plateau (Sicily). These consist of Al-diopside, pyralspite-series garnet, Al-spinel and Al-rich orthopyroxene. Trace element distribution resembles an enriched MORB but lower chromium. Major-element abundances closely fit in a tschermakitic-horneblende composition. Assuming that a high-Al amphibolite was formed by hydrothermal metasomatism of a troctolitic gabbro in a slow-spreading ridge segment, a transient temperature increasing induced dehydroxilization reaction in amphiboles, giving Al-spinel-pyroxenite and vapor as products. Garnet partially replaced spinel during an isobaric cooling stage. Density measurements at room conditions on representative samples gave values in the range 3290–3380 kg m^{-3}. In general, a density contrast ≥300 kg m^{-3} can give rise to convective instability, provided a sufficient large size of the heavy masses and adequate rheological conditions of the system. Garnet-pyroxenite lumps can therefore sink in the underlying mantle, imparting the "garnet geochemical signature" to newly forming basaltic magma.

Keywords: garnet-pyroxenite; amphibolite; gravitational instability; xenoliths; Sicily

1. Introduction

Garnet-bearing pyroxenites from ultramafic massifs and xenolith suites the world over can be due to crystal accumulation from mafic magmas at mantle depths, together with variable amounts of trapped interstitial magma [1]. Garnet is either considered a primary igneous phase [2–4] or product of reaction between pyroxene and spinel, due to variations in pressure and/or temperature conditions in the system [5,6]. Some garnet pyroxenites, generally called "recycled" [7], are instead thought to have origin from high-pressure metamorphism of crustal igneous mafic rocks during subduction events. Eclogites, as known, are typical recycled pyroxenites and their clinopyroxene component consisting of a jadeite-rich type [8]. The literature reports on other mechanisms leading to the formation of garnet-pyroxenites, such as subsolidus breakdown of a high temperature–high pressure subcalcic aluminous diopside [9] or dehydration-melting of amphibole-bearing metabasites, leaving garnet-pyroxenite as a restite product [6].

This paper deals with petrologic and mineralogical aspects of garnet-bearing pyroxenite xenoliths from diatreme-related tuff-breccia deposits in the Hyblean Plateau (Sicily, Central Mediterranean area). Even though the present results were chiefly based on a recent set of data, published and unpublished data acquired during a long-term research on the Hyblean xenoliths were also considered for discussion.

Results of this research also extend beyond the regional limits. Sizable amounts of garnet-pyroxenites are thought to occur at different depths in the convective mantle, in order to give reason to particular geochemical and isotopic characteristics of magmas related to spinel-facies mantle sources in different geological contexts worldwide, including oceanic islands and oceanic ridge segments [10]. Oceanic pyroxenites were considered either autochthonous products of the crystallization of partial melts at mantle depths [4,11] or allochthonous "recycled" crustal material, originated in subduction contexts and later involved in the convective motions of the mantle [7,10]. In the first case, it appears unclear why such a self-induced mantle metasomatism can confer exotic geochemical and isotopic signatures to partial melts from the same mantle source. In the latter case, it seems unlikely that recycled material, once formed in descending slabs, can be passively transported in the convective mantle for very long distances in space and time, with no severe melting and/or isotopic equilibration with the host mantle materials.

Have oceanic garnet-pyroxenites an "igneous-autochthonous" or a "recycled-allochthonous" origin? Results of the present study may cautiously shade some light on this problem, introducing the possible "recycled-autocthnous" origin of oceanic garnet pyroxenites, hence evaluating the role of garnet-pyroxenites in the development of convective instability in the oceanic mantle and possible "gravitational subduction" initiation.

2. Background Information

2.1. Geological Setting of the Hyblean Area

The Hyblean Plateau (Sicily, Southern Italy: Figure 1) consists of a tectonically uplifted sequence of deep-sea clayey and carbonate rocks, Upper Triassic to Miocene in age and open-shelf clastics Plio–Pleistocene in age, with intercalations of mafic volcanic rocks. The oldest sedimentary and volcanic rocks outcropping in this region date back to the Upper Cretaceous. Information on the stratigraphic succession prior to the Cretaceous Period comes from coring carried out during oil drilling. The main tectonic feature of the Hyblean Plateau consists of a NE-SW oriented system of extensional faults accommodated along a N-S trending right-lateral transform fault zone (Figure 1). Moreover, an active system of normal faults originated a steep submarine slope, the "Hybla-Malta Escarpment," that separates the Eastern Sicily from the Ionian abyssal plain.

There is no public-domain information on core-drill recovery of rocks from the pre-Triassic basement in the Hyblean Plateau, as well as in the entire Sicily mainland and its offshore areas, including the submerged Pelagian Shelf and Northern Tunisia [12]. Seismic data, including tomography models, on the Hyblean Plateau and surrounding areas, can be either compatible with a serpentinized oceanic lithosphere [13] or a delaminated continental crust [14]. Geological and paleontological investigations in Sicily and other Central Mediterranean areas [15], strongly indicate that the area corresponding to the present Sicily mainland was a broad deep-water basin in the Early Permian. Vai [15] suggested that such a deep marine basin was paved with oceanic crust, hence located along a trans-Pangea seaway, connecting the western Tethys to Panthalassa through the present Mediterranean, the NW Africa offshore and the Caribbean areas.

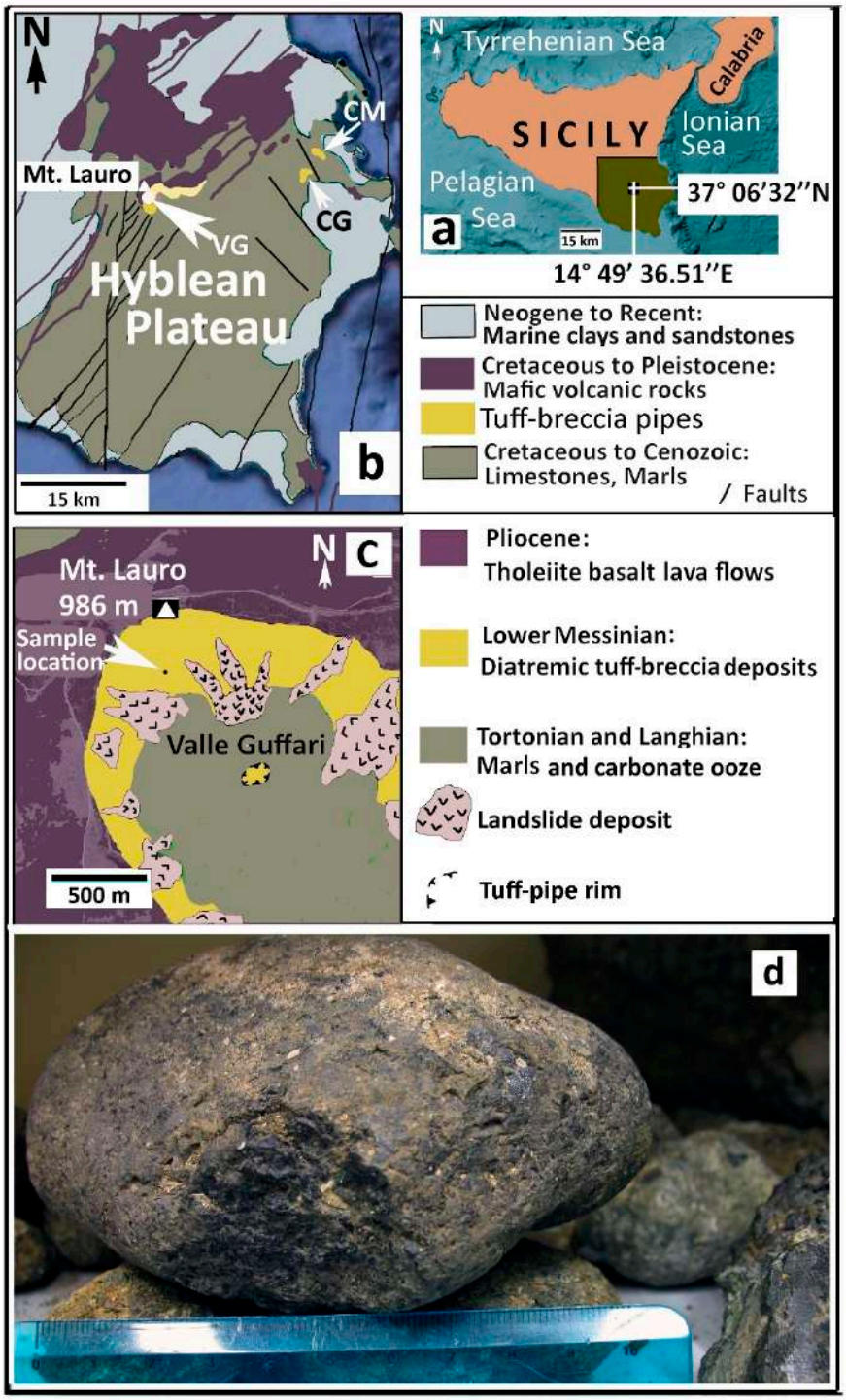

Figure 1. Location and geological setting of the xenolith-bearing diatremes and the sample. (**a**) General view of Sicily Island. The Hyblean Plateau area is highlighted by different color. Geographic coordinates indicate the sample location. (**b**) Geological sketch-map of the Hyblean Plateau. Arrows indicate the xenolith-bearing tuff-breccia deposits (CM = Cozzo Molino; CG = Costa Giardini; VG = Valle Guffari). The white circle indicates the sample location, in Valle Guffari. (**c**) Valle Guffari area with some detailed geological information. The arrow points to the sample location. The topography base was obtained from Google Earth. (**d**) Photograph of a garnet-pyroxenite xenolith from Valle Guffari, having almost the same size of the studied sample. The ruler is 10 cm in length.

The discovery of deep-seated xenoliths [16] in the Hyblean diatremes and their study over time, eventually confirmed the oceanic-lithosphere hypothesis. In particular, Scribano et al. [17] remarked that some gabbroic xenoliths closely resemble the oxide-rich tholeiite-gabbros with sheared texture typically occurring in oceanic settings with a slow-spreading regime, such as oceanic core-complexes (OCCs) and fracture zones [18]. In addition, the alteration products of both ultramafic and mafic xenoliths testify the occurrence of a long-lasting abyssal-type hydrothermal activity and extensive serpentinization in the Hyblean oceanic basement [19–21].

2.2. The Hyblean Volcanic Rocks

The volcanic activity in the area corresponding to the present Hyblean Plateau, as evidenced by outcropping products and drill-cores, developed discontinuously in submarine settings and on emerged parts of submarine volcanic edifices in Mesozoic and Cenozoic times. Triassic and Jurassic volcanic rocks were only recovered in subsurface [22]. The oldest outcropping volcanic products have an Upper Cretaceous age [23]. Most of the Hyblean volcanic rocks, Neogene–Quaternary in age, are exposed in the northeastern part of the Plateau (Figure 1), covering an area of about 350 km^2.

The Hyblean volcanic products exhibit both (Na) alkaline (alkali-basalts, basanites), high-alkaline (nephelinites) and subalkaline (tholeiite) affinity [24–28]. Trua et al. [27] highlighted the "geochemical paradox," that among the Hyblean volcanic rocks, both tholeiitic and alkaline basalts have isotopic compositions that are much more consistent with MORB-type magmas and trace-element concentrations that are more typical of ocean island basalt (OIB)-type magmas. The Sr-Pb-Nd isotopic signature of the entire Hyblean volcanic suite matches the volcanic rocks from the Mid-Atlantic-Ridge centered ocean island Ascension and the N. Atlantic MORBs [27]. Moreover, it is remarkable the absence, in the Hyblean volcanic rocks, of a geochemical component indicative of involvement of continental crust in the evolution of their magmas [27,29].

2.3. Hyblean Diatremes and Their Xenoliths

A few nephelinitic diatremes (Figure 1), Upper Miocene in age [30,31], brought to the surface, as a rule for such unusual eruptive systems, a number of xenoliths consisting of ultramafic rocks, compatible with mantle lithologies, mafic igneous intrusives, rare basalts and different sedimentary lithotypes. Hundreds of ultramafic and mafic xenoliths have been sampled since their discovery [32], of which about 65% are peridotites (spinel-harzburgites and rare lherzolites), 25% pyroxenites and the rest consists of grabbroids [33].

Scribano et al. [34] put forward, in a preliminary way, the hypothesis that the diatreme-forming explosive eruptions were due to the interaction between an upwelling mafic magma and shallow-seated serpentinites. Such a hypothesis was later addressed on a thermodynamic basis and validated by Manuella et al. [35]. Some pieces of information reported by Correale et al. [36] are also consistent with such a viewpoint. In this respect, it must be noticed that limestone xenoliths in the Hyblean diatremes show irregular shapes with sharp edges, as expected for mechanically broken fragments of such brittle rocks. On the contrary, ultramafic xenoliths have round shapes, both oval and sub-spherical, more consistent with a chemical rather than a mechanical process. For instance, the globular-type alteration of basalt bodies by aqueous fluids percolating along columnar joints eventually produces rounded basalt cores known as "onions," immersed in a clayey matrix, the smaller the globules the wider the alteration degree. Ultramafic xenoliths may therefore represent the least serpentinized relicts of the original ultramafic rocks, passively involved in the eruptive event. In other words, contrarily to the general thought that mantle xenoliths enter into diatreme systems at great depths, the Hyblean xenoliths derived from mantle rocks already tectonically uplifted at shallow crustal levels, even at seafloor and there widely serpentinized. The fully serpentinized fraction of the same rocks has been minutely fragmented and dehydroxylated during the explosive interaction with the upwelling magma and therefore it is no longer recognizable as such. The least serpentinized relicts, as mentioned, survived as xenoliths.

Scribano [37], following an established criterion [38], divided the Hyblean pyroxenites in two major groups on the basis of the composition of their clinopyroxene constituents, the Al-diopside and Cr-diopside groups. Hyblean pyroxenite xenoliths were studied by [33,37,39–45]. All these studies agree that the Hyblean pyroxenites are igneous cumulates formed at mantle depths. In particular, Nimis and Vannucci [39] concluded, on the basis of some trace element abundances, especially rare earth elements (REE), obtained by ion-microprobe analyses in clinopyroxenes from a highly unrepresentative set of samples, that the Al-diopside series derives from alkaline melts, whereas the Cr-diopside series can be attributed to tholeiite melts. This conclusion is the most accepted to date.

The occurrence of garnet in the Al-diopside series pyroxenites was first hypothesized by Punturo and Scribano [40] as microprobe analyses revealed that some enigmatic brownish patches, as appeared under the optical microscope, probably consisted of products from an almost isochemical breakdown of garnet (e.g., kelyphite). Atzori et al. [42] later provided plenty evidence of garnet relicts in samples from the same aluminous pyroxenite series. Further studies indicated that all Hyblean pyroxenite xenoliths larger than a fist, belonging to the Al-diopside group, bear at least a few crystal grains of garnet and/or its transformation products. In fact, garnet is easily overlooked due to its ubiquitous transformation into kelyphite which, in turn, is often extensively replaced by secondary minerals and/or affected by partial melting.

3. Materials and Methods

One third of the ~400 Hyblean xenolith samples collected by the authors of this paper over time consists of Al-diopside type pyroxenites. Thin sections from several pyroxenite xenoliths from the tuff-breccia deposits cropping out in the northern wall of Guffari valley (Figure 1) were preliminary observed under the optical microscope to identify the most representative sample. A relatively large xenolith, called (S), weighing 1.211 kg, was eventually chosen to be subjected to a more detailed study. The sample, as usual in the Hyblean pyroxenite xenoliths, exhibited an oval shape with a relatively smooth surface.

The sample was divided in four, almost equal, parts. One part was left intact to be archived for further study. Other portions (S1, S2, S3) were studied as independent samples. This fact in order to highlight possible inhomogeneity in the modal distribution of the bulk sample. In this respect, three thin sections were cut and polished in each sub-sample. In addition, several thin sections related to different samples from the same xenolith collection, already studied by the same author, were also revisited.

Analytical Methods

Optical microscope and scanning electron microscope (SEM), observation were made on standard (30 μm), polished, thin-sections of the three different parts of the sample. Mineral chemistry information was obtained by SEM fitted with energy dispersion system (EDS), microprobe fitted with wavelength dispersion system (WDS) and Laser-Ablation inductively coupled plasma mass spectrometry (LA-ICPMS). Whole rock chemistry was done via Inductively coupled plasma mass spectrometry (ICP-MS) and Inductively coupled plasma atomic emission spectroscopy (ICP-AES).

The used SEM was a TESCAN-VEGA\\LMU SEM (Brno, Czech Republic) equipped with an EDAX Neptune XM4 60 (Berwyn, PA, USA) microanalysis working in energy dispersive spectrometry (EDS), at the Catania University (Italy). Observations were made in backscattered electron mode under high vacuum conditions at accelerating voltage 20 kV and beam current 0.2 nA. Qualitative analyses were performed on thin sections and fragments of the sample with plane and semi-polished surfaces. Wavelength-dispersive analyses of major elements of diverse minerals were performed using the JEOL JXA 8230 (Akishima, Tokyo, Japan) electron probe micro-analyzer (EPMA) at the Department of Biological, Ecological and Earth Sciences of the Università della Calabria (Cosenza, Italy). Calibrations were carried out using native metals and silicates as standard materials. Analyses were obtained under the following instrumental conditions: an accelerating voltage of 15 kV, a beam current of

10 nA, a beam spot of 5 μm and an analysis time of 100 s. A detection limit of 0.01 wt.% is for all the detected elements.

Micro-Raman spectra on representative garnet grains and their kelyphite rinds have been acquired at Catania University through a Raman Jasco NRS-3100 apparatus (Halifax, Nova Scotia, Canada), equipped with a microscope with ×10, ×20 and ×100 objectives, using a laser excitation source at 532 nm; laser power has been controlled by means of a series of density filters, in order to avoid heating effects. Depth resolution was set to few micrometers by means of a confocal hole. The system has been calibrated using the 520.7 cm^{-1} Raman band of silicon before each experimental session.

Whole rock chemical analyses were performed on selected portions of the three parts (S1, S2, S3) of the sample (S), which were crushed and powdered with an agate mortar. Weighted aliquots were sent to the commercial laboratory of SGS (Lakefield, Ontario, Canada). The powdered samples were there analyzed by ICP-AES and ICP-MS technical procedures the accuracy of the methods was determined by analyzing certified reference materials, while their precision was determined with replicate analyses and found to be generally better than 10%. Further information on the analytical methods, including details in accuracy and precision of the standards used, can be found at the following link: https://www.sgs.com/-/media/global/documents/brochures/sgs-analytical-guide.pdf.

In situ trace-element analyses were performed in key minerals and bulk kelyphite by laser ablation (LA)-ICPMS technique at Istituto Nazionale di Geofisica e Vulcanologia (INGV) in Palermo. Polished thin sections, of about 80 μm in thickness, were cut from the three different parts of the sample. The analytical system consisted of an Agilent-7500 CX (Santa Clara, CA, USA) quadrupole mass spectrometer coupled with an ArF excimer laser ablation system (GeoLas Pro, Coherent, Inc., Santa Clara, CA, USA). During analysis, samples were maintained in a helium atmosphere, with a laser output energy of 10 J/cm^2, a repetition rate of 10 Hz and a 130 μm diameter circular spot. Ca, Si and Fe as internal standards and NIST 612 as an external standard were used. The NIST 612 analyses were carried out at the start, middle and end of each analytical session. The precision was determined during each analysis session from the variance of ~15 NIST 612 measurements, which gave a relative standard deviation of ~5%. The accuracy, calculated using the BCR-2 international standard, was ~10% for most of the elements.

Density measures were performed on representative powdered portions of the sample by the means of a pycnometer and a 0.1 mg accuracy electromagnetic balance, using bi-distilled water as medium. The density of the sample was determined at 22.4 °C and of the water at 4 °C, at a nominal pressure of 101.325 kPa. It has been carefully checked for air bubbles in the bulb or capillary of the pycnometer and no air space at the top of the capillary, before each measurement.

4. Results

4.1. Optical and SEM Petrography

The sample mineral assemblage consists of clinopyroxene (Cpx), widely kelyphitized garnet (Grt), Al-rich spinel (Spl), orthopyroxene (Opx), very rare zircon and moderate amounts of alteration minerals, such as zeolites and smectites. At the hand specimen all minerals display black or dark-gray color, except the garnet relicts, which appear as tiny, semi-transparent grains yellowish-brown in color. Thin sections study indicates that the modal distribution of major minerals, as well as their grain size, vary irregularly at the sample scale. The average modal distribution (vol%) of the major minerals, on the basis of the full set of thin sections extracted from the three fragments of the sample, is the following: Cpx ~65%; Grt (+ kelyphyte)~20%; Spl ~10 vol%; Opx ~5%.

The coarse-grained parts of the rock consists of equant, anhedral clinopyroxene grains, 3–5 mm in size, tightly juxtaposed according to irregular, curvilinear grain-boundaries (Figure 2a) with minor amount of garnet (Figure 2b), finer-grained orthopyroxene and Al-spinel grains. The latter exhibit subrounded shape (Figure 3a,b). Clinopyroxene and garnet (often totally replaced by kelyphite) grains in some cases appear deeply embayed. The garnet "fingers" locally sharply "cut" the pyroxene

cleavage traces, as shown in Figure 2c. The less coarse areas of the sample, as observed in thin section, consist of clusters of clinopyroxene grains, 0.3–1 mm in size, with curvilinear, even sub-rounded, grain boundaries, immersed into the kelyphite, together with rounded, opaque, Al-spinel grains and irregular, colorless relicts of the original garnet (Figure 2e,f). Such a configuration recalls either a poikylitic or poikyloblastic texture. The coarse and fine grained areas are irregularly interfingered (Figure 2e,f).

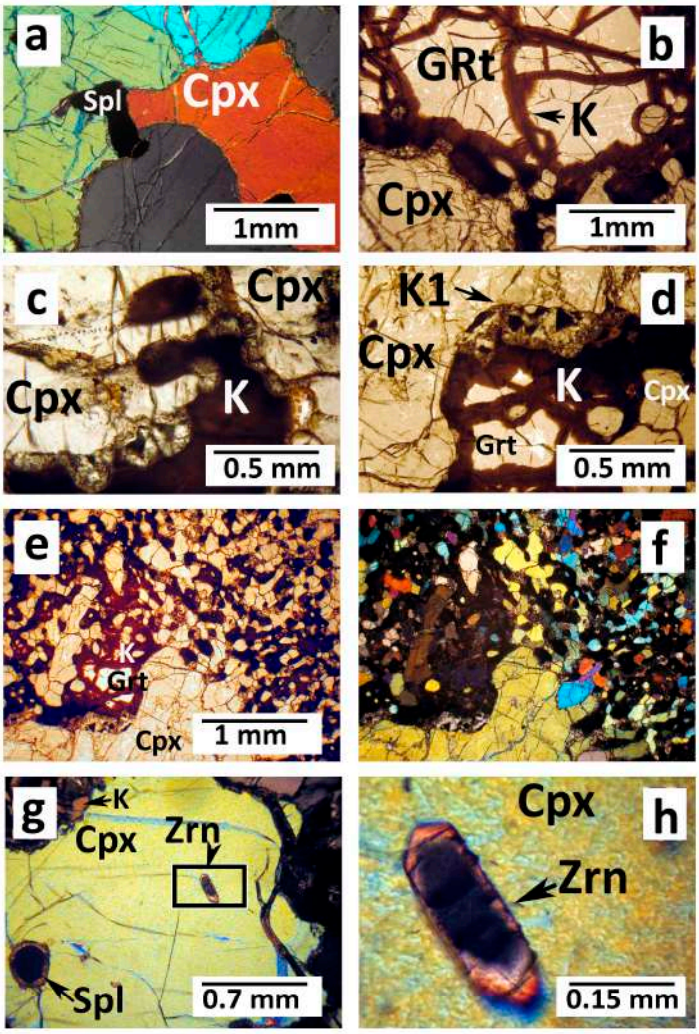

Figure 2. Microphotographs displaying details of sample thin sections under the optical microscope, in plane polarized transmitted light. (**a**) Geometric relationships between coarse clinopyroxene (Cpx) grains. Crossed polars. Spl = Al-spinel. (**b**) Coarse garnet grain (Grt) partially replaced by kelyphite (K). Plane pol. light. (**c**) Penetrative intergrowths between kelyphite, replacing former garnet and clinopyroxene. Plane pol. light. (**d**) Detail of a typical curvilinear contact between coarse clinopyroxene (Cpx) and garnet (Grt). The garnet is widely replaced by kelyphite. The arrows indicate a zone of the contact surface where the grain-size of the kelyphite is significantly increasing (K1). Plane polarized light. (**e**) Microphotograph (plane polarized light) showing the passage between the coarse- and fine-grained areas of the sample. The former is represented by a small portion of a coarse clinopyroxene grain (bottom side of the picture). The fine-grained area exhibits a poikyloblatic-like texture consisting of irregular garnet relicts, small round clinopyroxene and spinel grains immersed in the kelyphite (dark brown to black in color). (**f**) The same as in (**e**) viewed under crossed polars. (**g**) A clinopyroxene grain enclosing a tiny, euhedral zircon grain (Zrn). Plane polarized light, crossed polars. (**h**) Magnification of the rectangular inset in the previous picture highlighting the zircon grain. More explanation is given in the text.

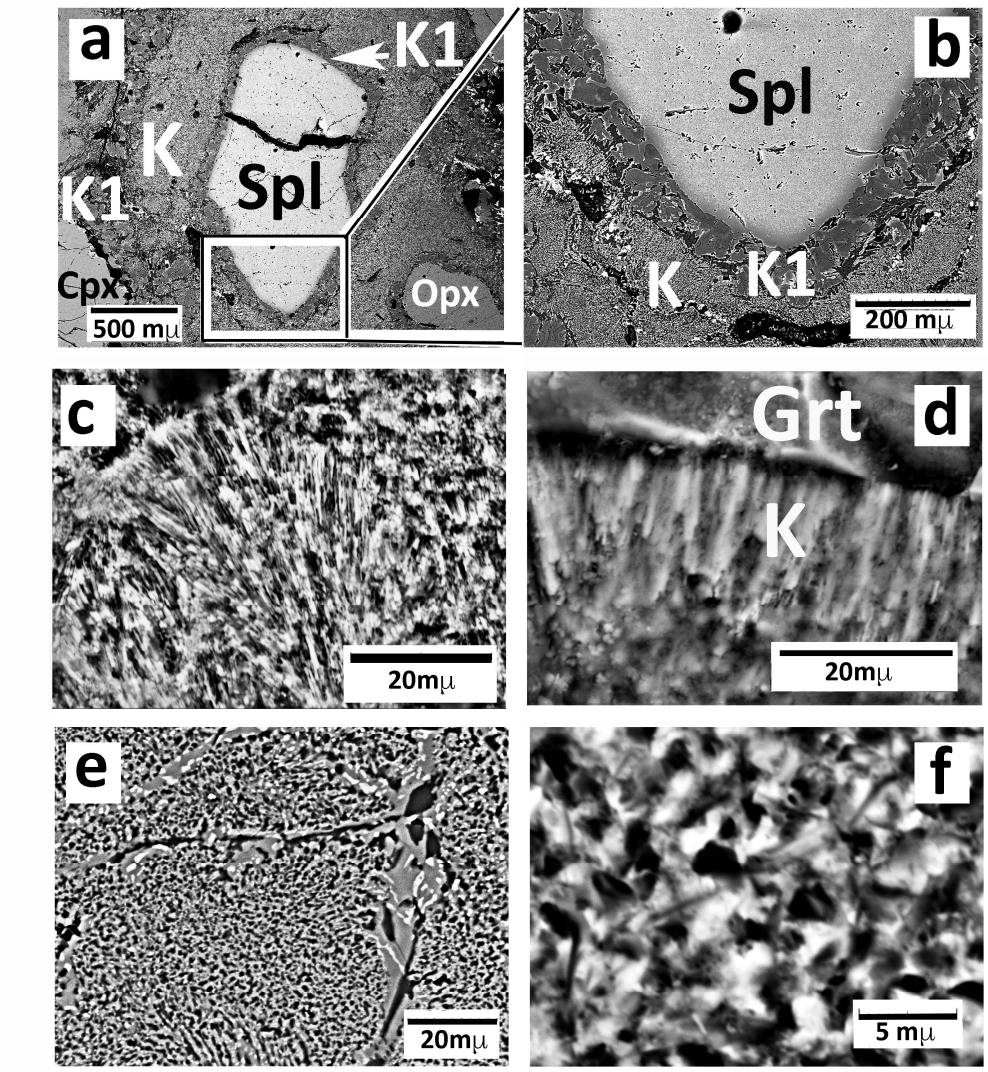

Figure 3. Scanning electron microscopy (SEM) images in backscattered electron mode (BSE) showing details of thin-sections and fragments of the sample highlighting typical kelyphite textures. (**a**) Typical Al-spinel grain (Spl), with rounded edges, immersed in the fine kelyphite (K), which fully replaces former garnet. A collar of coarser-grained kelyphite (K1) occurs around the spinel and nearby clinopyroxene (Cpx) and orthopyroxene (opx) grains. The area enclosed in the rectangular inset is displayed in figure (**b**) at higher magnification. (**c**) 3-D view of the fine kelyphite in a small fragment of the sample. Bright mineral is spinel, dark gray is ortophyroxene, most of the black spots are void volumes. (**d**) The same as in (**c**) showing the sharp passage between kelyphite and the fresh garnet (Grt). (**e**) Kelyphite as it appears in thin section. Clear areas consist of spinel, gray areas mostly consist of Ca-poor pyroxene, dark area are either Ca-rich plagioclase, alteration products of plagioclase or empty spaces. (**f**) High magnification of the kelyphite evidencing porosity, as the dark spots mostly consist of void spaces.

As already mentioned, kelyphite (K) replaces, to a large extend, garnet. Under the optical microscope kelyphite areas display color zoning from deep brown to almost opaque, with a weak birefringence with anomalous interference color. The undulatory extinction highlights the flaky texture of the kelyphite. The kelyphitization process proceeded from rim to core, along fractures of the garnet grains (Figure 2b,d). The kelyphite, as it appears in tiny fragments under the scanning electron

microscope, consists of juxtaposed, roughly conical bunches of elongated crystals or crystallites, several micrometers in length, less than one micrometer in width. There are empty spaces between the minerals (Figure 3c,d). Spot analyses with a tightly focused beam in polished and coated thin sections, qualitatively indicate that the kelyphite minerals consist of Ca-poor pyroxene, Al-spinel, Ti-magnetite and an interstitial matter with a fibrous appearance. SEM observation at highest magnification mode shows that the kelyphite mineral assemblage gives rise to very fine pores (Figure 3f), which correspond to the "empty tubes" as seen in a 3-D perspective (Figure 3c,d).

The grain size of the kelyphite increases significantly nearby the contact with spinel grains (Figure 3a,b and Figure 4a). Such a coarse kelyphite appears as an interlocked assemblage of Ca-poor pyroxene and Al-spinel micrograins, 5–25 micrometers in size, enclosing smaller micrograins (1–3 micrometers) of anhedral Ti-magnetite. Rare Ca-rich plagioclase is interstitial between pyroxene and spinel. The kelyphite Al-spinel micrograins, which are always anhedral in the fine areas, often appear subhedral, even euhedral, in the coarse zones. Coarsening of the kelyphite grain-size also locally occurs along the clinopyroxene grain boundaries, only nearby the outlet of pyroxene microfractures filled by brownish, clayey matter (Figure 2d).

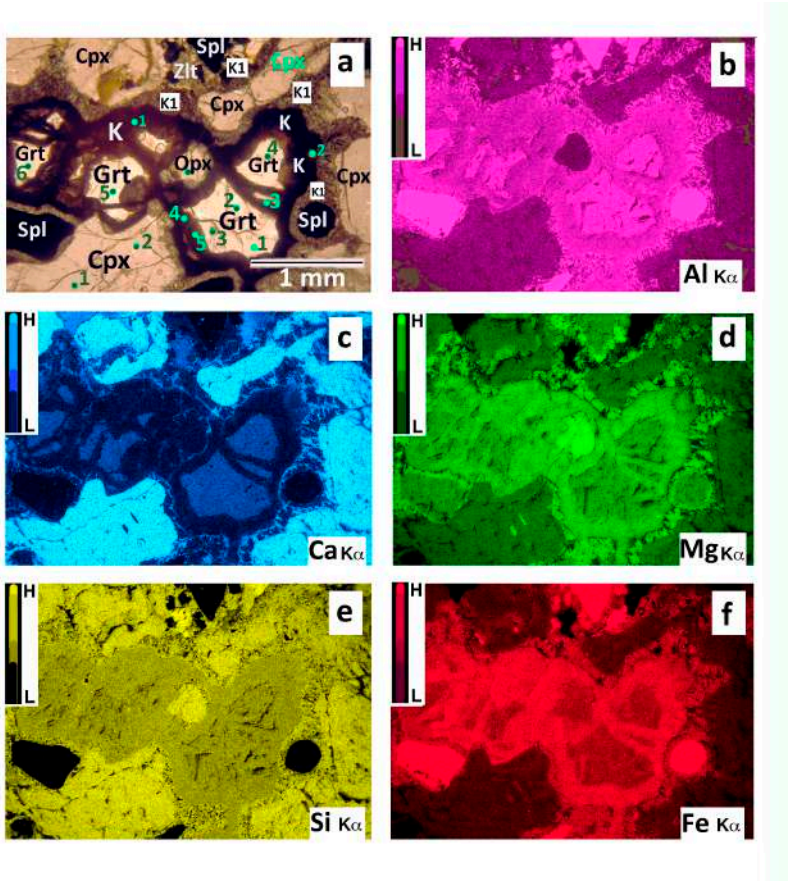

Figure 4. Dispersive energy spectrometer (EDS) chemical maps of a representative area of a polished section of the sample. Intensity of colors is proportional to the respective element abundances. (**a**) View of the area under the optical microscope (plane pol. transmitted light). Cpx = clinopyroxene; Grt = garnet; K = fine-grained kelyphite (replacing garnet); Opx = orthopyroxene; Spl = Al-spinel; K1 = coarse kelyphite (around spinel and pyroxenes); ZTL = Ca-K zeolite. Numbered circles in the mineral grains indicate location of Laser_ablation spot analyses. More explanation is given in the text. (**b**) Al chemical map. (**c**) Ca chemical map. (**d**) Mg chemical map. (**e**) Si chemical map. (**f**) Fe chemical map.

In only one of the fifteen thin-sections obtained from the sample, a few tiny euhedral crystals (Figure 2e,f), whose optical characteristics perfectly fit in a zircon, appear included in coarse clinopyroxene grains.

Hydrous secondary minerals, consisting of colorless zeolites, with low-order interference colors and yellowish smectites are ubiquitous in the sample, often filling tiny irregular vesicles between the primary mineral grains (Figure 4a). Zeolite and smectite are always associated in the same vesicle.

4.2. Chemistry of Minerals and Bulk Kelyphite

The relative abundances of selected major elements in the essential minerals of the sample, also in the kelyphite and symplectites, is comprehensively, although qualitatively, indicated in the EDS chemical maps reported in Figure 2b–f. Specific information on the sample mineral chemistry is given below.

Clinopyroxene is an aluminum diopside ($45.30 < En\ mol\% < 48.80$; $0.390 < Al\ a.p.f.u. < 0.469$) according to Morimoto [46]. The mafic index $100 \times Mg/(Mg + \sum Fe)$, indicated as Mg#, varies between 74 and 77. The clinopyroxene end member calculation following Papike [47] indicates high abundance of the Ca-Tschermakite component. Both coarse and fine clinopyroxene grains do not display core-to-rim composition variations. Representative microprobe analyses on clinopyroxene are reported in Table 1.

Table 1. Major element abundances of the whole rock samples (S1, S2, S3), theirs average values (S) and the constituent minerals (Calcic pyroxene: Cpx, Ca-poor pyroxene: Opx, garnet: Grt and Al-spinel: Spl). Composition of a square area (Raster), with 75 mm long side, of the fine grained kelyphite (K) and spot analyses on the Ca-poor pyroxene and plagioclase (Plag) in the coarse kelyphite (K1), are also reported.

	Calcic Pyroxene				**Ca-Poor Pyroxene**		
wt%	Cpx a	Cpx b	Cpx c	Cpx d	Opx a	Opx b	OpxK1
SiO_2	49.52	49.51	48.48	49.40	51.23	52.86	49.71
TiO_2	1.56	1.56	1.59	1.75	0.54	0.09	0.00
Al_2O_3	9.27	9.15	9.52	9.30	6.89	7.00	10.28
FeO*	7.78	7.75	7.81	7.55	12.53	12.71	12.95
MnO	0.03	0.00	0.08	0.01	0.18	0.11	0.00
MgO	13.68	14.16	13.54	13.76	27.20	25.55	24.90
CaO	16.73	16.35	17.81	16.77	1.35	1.88	2.14
Na_2O	1.45	1.51	1.41	1.50	0.19	0.05	0.00
Total	100.02	99.99	100.24	100.02	100.11	100.25	99.98
	Garnet				**Kel(K) Plag**		
wt%	Grt a	Grt b	Grt c	Grt d	Grt e	RASTER	(K1)
SiO_2	42.97	44.24	44.02	42.09	41.99	41.38	45.16
TiO_2	0.70	0.73	0.81	0.54	0.56	0.69	0.00
Al_2O_3	20.48	19.77	20.94	22.78	23.50	18.01	34.01
FeO	12.79	12.52	11.28	12.04	12.05	16.16	1.55
MnO	0.28	0.35	0.37	0.34	0.20	0.57	0.00
MgO	17.50	16.99	16.09	16.17	15.01	22.23	1.06
CaO	5.31	5.34	6.57	5.98	6.33	1.10	17.23
Na_2O	0.00	0.00	0.00	0.00	0.00	0.12	0.74
K_2O	0.00	0.00	0.00	0.00	0.00	0.02	0.00
Total	100.03	99.94	100.08	99.94	99.44	100.28	99.75
	Spinel				**Whole Rock (S)**		
wt%	Spl a	Spl b	Spl c	S 1	S 2	S 3	**S[Av]**
SiO_2	0.42	0.00	0.30	40.64	41.71	42.35	**[41.54]**
TiO_2	1.09	1.06	0.33	1.53	1.48	1.48	**[1.50]**
Al_2O_3	57.17	57.20	61.23	16.01	16.19	15.77	**[15.99]**

Table 1. *Cont.*

FeO	23.08	23.71	19.33	9.85	9.73	9.43	**[9.65]**
MnO	0.00	0.00	0.00	0.10	0.13	0.13	**[0.12]**
MgO	17.68	18.03	18.13	15.12	14.35	13.48	**[14.45]**
CaO	0.00	0.00	0.00	12.59	13.15	12.31	**[12.70]**
Na_2O	0.00	0.00	0.00	1.06	1.06	1.10	**[1.07]**
K_2O	0.00	0.00	0.00	0.00	0.00	0.12	**[0.05]**
P_2O_5	0.00	0.00	0.00	0.06	0.09	0.13	**[0.10]**
Total	99.44	100.00	99.32	96.96	97.89	96.29	

Clinopyroxene trace element distribution, obtained by LA-ICPMS spot-analyses, is reported in Table 2. Chromium content is low (Cr~25 ppm). The compatibility diagram normalized to Primordial Mantle (PM) [48] shows an upward-convex pattern (Figure 5), due to depletion of both highly incompatible (except Li, Be and Cs) and highly compatible elements (e.g., Cr, Ni) with respect to PM values. Moderately compatible elements generally not exceed 10 × PM values. The pattern shows more or less pronounced negative anomalies with respect to Nb, Pb, Ho, Co and Cr. The sum of REE is about 46 ppm. REE distribution normalized to chondrite CI [49] displays a moderately upward-convex pattern, with a relatively long descending limb (Figure 6).

Table 2. Trace element abundances of the sample whole rock (S), garnet (Grt), kelyphite (K), clinopyroxene (Cpx) and Ca-poor pyroxene (Opx). The whole rock is the average composition of three different fragments of the sample. Analyses of minerals and kelyphite are representative Laser-Ablation spots. nd = not detected.

	S	Grt1	Grt2	Grt3	Kel1	Kel2	Kel3	Cpx1	Cpx2	Opx1	Opx2	Spl1
ppm												
Li	<10	<1.5	<1.5	<1.5	30.88	20.04	4.05	2.31	2.46	3.66	4.28	5.44
Be	<5	<0.8	<0.8	<0.8	8.02	11.92	1.23	<0.6	0.65	<0.6	<0.6	0.00
B	nd	<1.14	<1.06	<1.15	68.03	33.20	8.09	<0.72	<0.80	<1.63	<1.66	0.00
Sc	35	105.36	104.55	105.07	1570.10	1229.39	245.62	34.95	35.26	35.77	35.56	1.06
Ti	9000	3401	3395	3285	4848	3484	7706	11726	12068	7813	8085	9313
V	353	139.68	138.80	136.86	2145.77	1402.37	360.36	393.16	400.70	448.88	461.18	1377
Cr	94.33	32.04	30.24	32.74	524.61	313.22	73.45	24.86	25.12	39.03	38.35	626
Co	85.27	76.58	77.75	78.95	1167.63	796.35	192.5	47.97	48.96	223.42	228.90	717
Ni	252	20.51	19.29	19.44	607.71	339.23	67.35	96.90	102.11	395.76	412.48	2080
Cu	44.67	1.81	0.71	1.29	338.77	265.57	26.96	4.69	1.81	2.10	1.88	2.55
Zn	156	37.65	37.60	36.32	967.25	809.32	131.14	41.18	42.30	216.35	211.58	31.06
Rb	2.55	0.12	0.05	0.04	49.31	14.86	26.56	0.09	0.02	<0.03	<0.02	0.00
Sr	185.67	0.31	0.34	0.44	357.09	257.55	238.9	87.53	87.26	1.54	1.56	0.10
Y	19.67	72.83	73.72	71.10	829.99	643.10	148.03	15.53	15.01	3.19	3.22	0.00
Zr	44.10	45.92	43.93	42.41	564.90	455.80	104.09	40.50	39.76	10.48	11.30	0.16
Nb	3.67	0.07	0.06	0.03	2.22	0.63	0.063	0.51	0.50	0.09	0.08	0.00
Cs	0.73	<0.01	<0.01	<0.01	5.28	1.80	0.319	0.02	<0.01	<0.01	<0.01	0.00
Ba	157.33	0.18	0.21	0.59	75.49	41.93	1908.09	0.60	0.26	0.38	0.13	0.00
La	5.53	0.01	0.02	0.02	0.53	0.53	0.053	3.36	3.22	0.03	0.06	0.00
Ce	14.30	0.24	0.21	0.22	2.70	2.02	0.253	12.60	12.66	0.23	0.24	0.00
Pr	2.10	0.09	0.11	0.10	0.30	0.29	0.104	2.12	2.16	0.04	0.04	0.00
Nd	10.17	0.98	0.97	1.16	8.56	5.64	1.27	11.79	11.90	0.36	0.43	0.00
Sm	3.13	1.33	1.27	1.16	9.59	7.65	1.38	4.03	3.62	<0.1	0.27	0.00
Eu	1.35	0.78	0.78	0.83	0.95	1.37	0.54	1.30	1.24	0.08	0.11	0.00
Gd	3.84	4.41	4.10	3.83	34.69	30.01	7.12	4.23	3.97	0.29	0.47	0.00
Tb	0.59	1.12	1.14	1.08	9.25	8.56	1.89	0.54	0.63	0.08	0.06	0.00
Dy	3.96	10.63	10.04	10.08	103.42	89.62	20.29	3.61	3.56	0.63	0.56	0.00
Ho	0.76	2.72	2.64	2.69	31.61	25.19	5.55	0.63	0.64	0.11	0.13	0.00
Er	2.05	9.08	9.03	8.71	114.58	91.85	20.53	1.48	1.39	0.30	0.37	0.00

Table 2. *Cont.*

	S	Grt1	Grt2	Grt3	Kel1	Kel2	Kel3	Cpx1	Cpx2	Opx1	Opx2	Spl1
Tm	0.31	1.55	1.47	1.45	19.91	13.60	3.21	0.15	0.15	0.08	0.04	0.00
Yb	1.77	10.89	11.31	9.87	145.54	104.14	25.05	0.84	0.86	0.43	0.35	0.00
Lu	0.36	1.65	1.79	1.73	24.03	18.84	3.99	0.14	0.12	0.07	0.06	0.00
Hf	1.67	0.88	0.76	0.65	11.17	6.78	1.87	1.53	1.51	0.31	0.48	0.12
Ta	0.00	0.02	<0.01	<0.01	0.11	<0.07	<0.006	0.08	0.10	0.03	<0.02	0.00
Pb	0.00	0.15	0.11	0.18	2.27	1.59	0.51	0.12	0.13	<0.09	<0.16	0.29
Th	0.33	<0.02	<0.01	<0.02	<0.20	0.44	<0.016	0.06	0.04	<0.02	<0.02	0.00
U	0.13	<0.02	<0.02	<0.03	<0.25	<0.23	0.021	0.01	0.01	<0.03	0.10	0.00

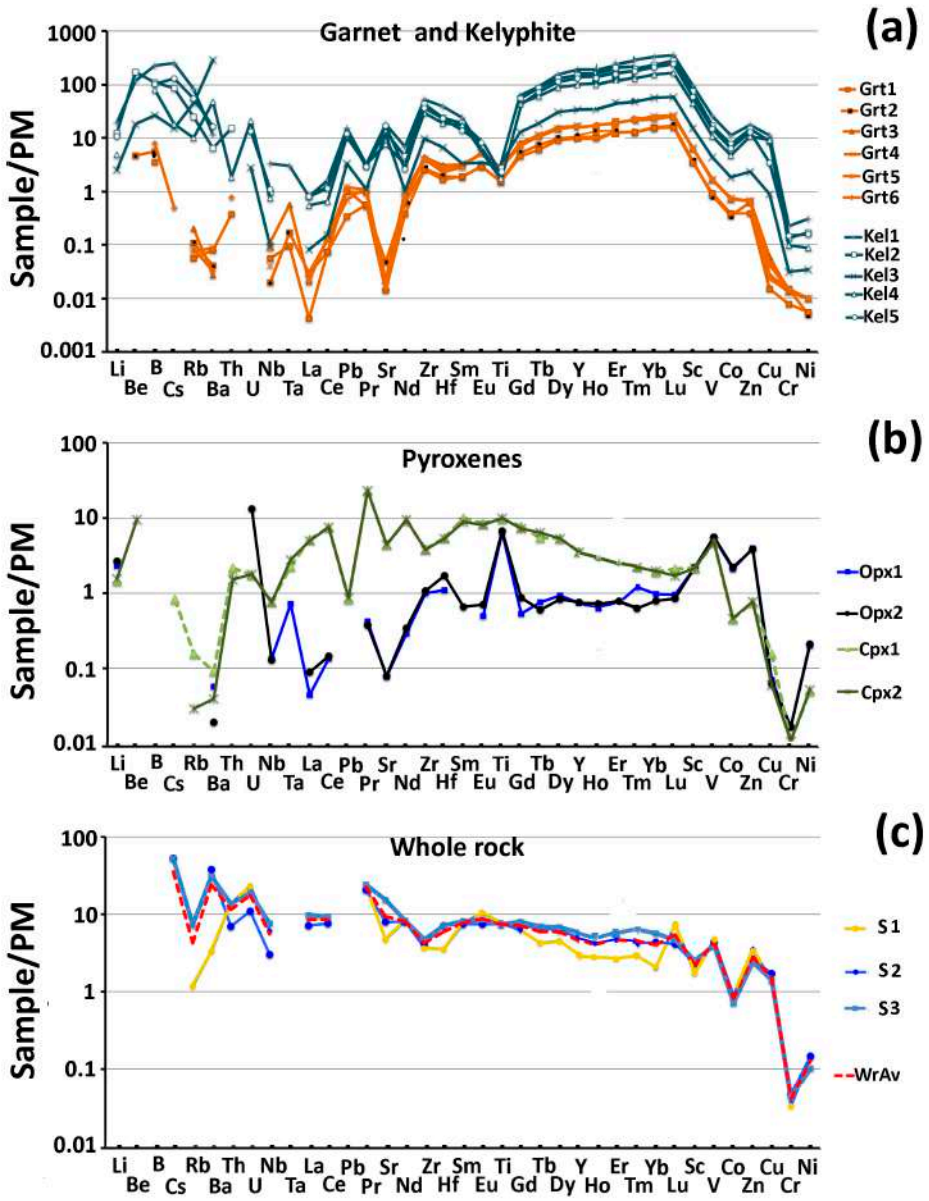

Figure 5. Multielement distribution patterns normalized to primordial mantle composition (PM) [48] of the sample whole rock and garnet, kelyphite and pyroxenes compositions. (**a**) Results of Laser-Ablation spot analyses on garnet grains (Grt1–Grt6) and Kelyphite (K1–K5). (**b**) Representative compositions of clinopyroxene (Cpx) and Ca-poor pyroxene (Opx). Numbers correspond to spot analyses as indicated in Figure 2a. (**c**) Whole-rock composition of sub-samples S1, S2, S3 and their average values (WrAv). More explanation is given in the text.

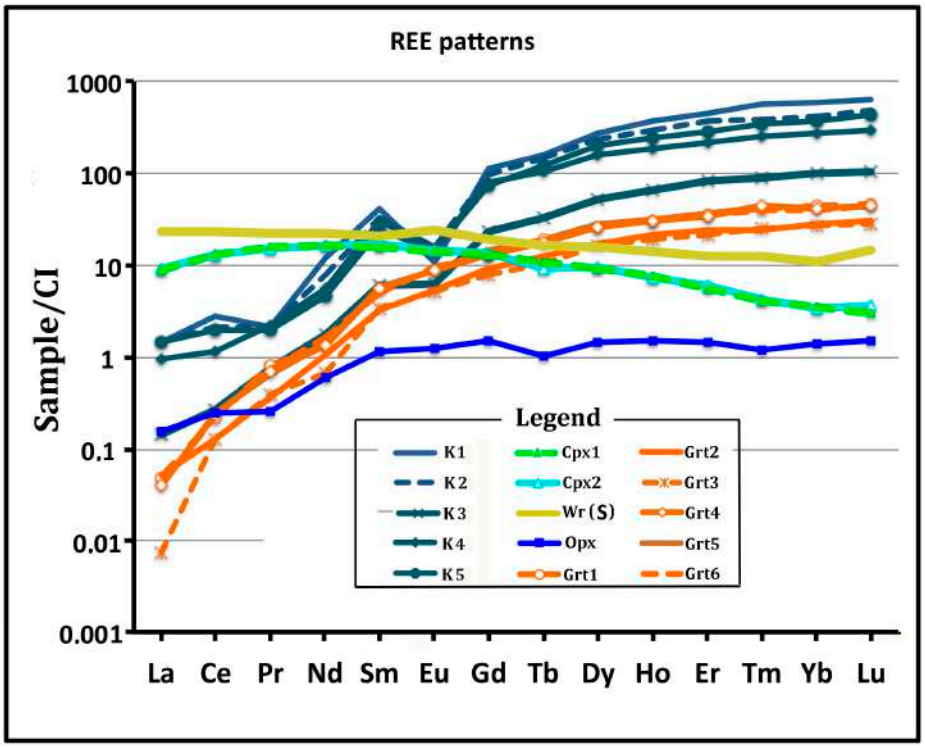

Figure 6. CI-normalized [49] rare earth element (REE)patterns of the sample whole rock (Wr-S) and therein garnet (Grt1–Grt6), Kelyphite (K1–K5), Calcic pyroxene (Cpx1 and Cpx2) and Ca-poor pyroxene (Opx). Numbers correspond to spot analyses as indicated in Figure 4a.

Orthopyroxene is found both as small rounded grains immersed in the kelyphite (Figure 4a) and anhedral subgrains, up to 1.5 mm in size, nearby coarse clinopyroxene grains. The same Ca-poor pyroxene also form exsolution lamellae or micrograins in the clinopyroxene. In some cases, both exsoluted ortopyroxene and the nearby coarse subgrains display coherent extinction. In addition, Ca-poor pyroxene is the dominant mineral phase in the kelyphite. Microprobe analyses in the exsolution lamellae and in the kelyphite ultra-micrograins are biased by their small grain size with respect to the beam width. The sample orthopyroxene grains generally show an enstatite-rich composition: En (mol%) = 75–82, Fs = 13–21, Wo = 3–5, with high content in aluminum (Al_2O_3 = 6–9 wt%). Orthopyroxene micrograins in the coarse kelyphite areas has an Al_2O_3 content as high as ~12 wt% (Table 1). CaO is less than 2 wt%. Some trace elements, as Nb, light REE (LREE), middle REE (MREE), Sr, Ba, Cr and Ni are depleted at various extend with respect to PM values (Figure 5). Moderately compatible elements display approximately PM composition, whereas Ti, V, Co and Zn are slightly enriched with respect to PM composition (Figure 5). The sum of the orthopyroxene REE is ~3 ppm and their CI-normalized pattern (Figure 6) displays a gentle uphill slope.

Garnet relicts, always immersed in the kelyphite, have a relatively uniform composition. Pyrope is the most abundant end-member, 57< Py (mol%) <64, followed by almandine, 23< Alm (mol%) <25, whereas the Ca and Mn end-members vary between 13 and 15 mol% and 0.5 to 1 mol%, respectively. Trace element distribution of five representative spot analyses (Figure 4a) were normalized to PM values and reported in Figure 5. Incompatible element abundances, including LREE, are lower than PM values, with negative anomalies in La and Sr, whereas compatible element abundances generally exceed PM values. Elements from V to Cr are much less abundant than PM. The REE distribution normalized to CI values displays the typical uphill-trending slope of garnets (Figure 6).

The micro-Raman spectrum of the garnet, as reported in Figure 7a,b, displays three main peaks at 358, 558 and 919 cm^{-1}, respectively, the latter being the highest. and three weak bands, just above the background noise, at 646, 862 and 949 cm^{-1}. The main triplet is typical of all silicate garnets,

as it is attributed to rotational, internal bending and stretching vibrations of the SiO_4-tetrahedra, respectively [50]. In particular, the spectrum morphology best fits in a pyrope-rich member of the pyrope–almandine–spessartine (pyralspyte) garnet series, with minor amount of grossular [51,52]. This is consistent with the garnet mineral chemistry as reported in Table 1.

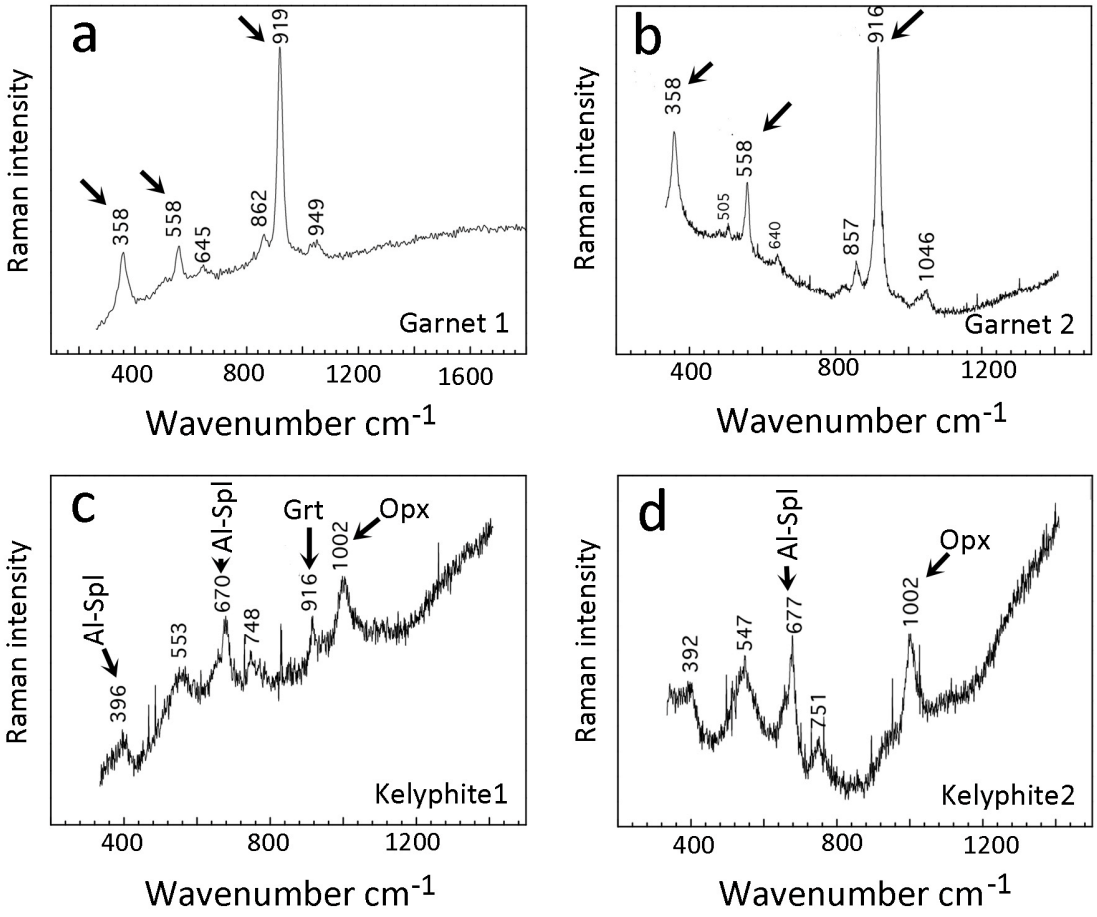

Figure 7. Micro-Raman spectra of garnet grains (**a**,**b**) and tiny portions of fine kelyphite (**c**,**d**). Full explanation is reported in the text.

Garnet, as already mentioned, is widely replaced by *kelyphite*. The kelyphite bulk composition, as obtained by raster microprobe analyses in square areas with 75 micrometers side-length, matches the original garnet but lower content in calcium (Table 1). This circumstance is evident in the Ca chemical map reported in Figure 4c. Laser Ablation spot analyses in different kelyphitized areas (Figure 4a) highlight significant variations in trace elements composition with respect to the original garnet. Multielement diagram normalized to PM composition (Figure 5) indicates that the kelyphite is enriched in highly incompatible elements, including fluid mobile elements (FME). Lithium, always below detection limits in the garnet, is here enriched up to 12 × PM; Be up to 100 × PM; B and Ba are both enriched up to 200 × PM; U, which is below detection limits in the garnet, is enriched up to 12 × PM in the kelyphite. The sequence of elements from Nb to Ni displays a roughly similar pattern as the garnet but higher absolute contents and a slightly positive anomaly in Sr, which is negative in the garnet. About the REE distribution, the CI-normalized REE patterns relative to different kelyphite spot analyses display an upward slope, according to the garnet but absolute abundances in both LREE and HREE higher than garnet (Figure 5). Notably, contrary to garnet, the REE kelyphite patterns display evident negative Eu anomaly. This can be numerically indicated by the ratio Eu_N/Eu^* (= 0.28, on average), where $Eu^* = (Sm_N + Gd_N)/2$ [53].

Raman spectra, related to two different areas of the kelyphite, as indicate in Figure 4a, display (Figure 7c,d) elevated background noise which can be ascribed to the occurrence of very fine grained, hence poorly crystalline, material. The spectrum reported in Figure 7c displays a weak band at 916 cm^{-1}, which most probably is related to disequilibrium relicts of the original garnet. The peak at 1002 cm^{-1} indicates a Mg-rich, Ca-poor pyroxene [54], whereas peaks at around 390 and around 370 cm^{-1} are probably related to an Mg-Fe-aluminous spinel [55]. The weak peaks around 550 and around 750 cm^{-1} (Figure 7d) cannot be unambiguously attribute to a given mineral as they are either compatible with different silicates, including Ca-rich plagioclase [56] and clay minerals [57].

Spinel is an aluminous type, Al_2O_3 being in the range 57–61 wt% (Table 1). FeO (total iron) is in the range 19–24 wt%, MgO varies between 17 and 18 wt%, TiO_2 between 0.3 and 1 wt%. The average formula (a.p.f.u.) is the following: Si = 0.006, Ti = 0.016, Al = 1.799, Fe^{3+} = 0.156, Fe^{2+} = 0.325, Mg = 0.698, where Fe^{3+} is calculated from charge balance. About trace element distribution, only V (~1300 ppm), Cr (~600 ppm), Co (~700 ppm) and Ni (~2000 ppm) occur in sizable amounts (Table 2). No composition variations related to the spinel grain size, including the kelyphite spinel, has been detected.

The *zeolite* that fills vesicles sparse in the rock, together with smectites, is a Ca-K-Ba-rich type., There is no information on the *zircon* mineral chemistry so far, as the thin-section where the zircon grains occur is, unfortunately, apt for optical observation only.

4.3. Whole Rock Chemistry

The three sub-samples S1, S2 and S3 (see above) display variations in major elements generally within the analytical error (Table 1), except for silica (SiO_2 = 40.64 wt% in S1, 41.71 wt% in S2 and 42.35 wt% in S3) and magnesia (MgO = 15.12 wt% in S1, 14.35 wt% in S2, 13.48 w% in S3). Considering the average values (S) with respect to the three sub-samples, it must be highlighted the relatively high content in a aluminum (Al_2O_3~16 wt%) of this rock with respect to its low silica (SiO2 = 41.5 wt%) and high MgO (= 14.4 wt%) abundances. The content in alkalis is low (Na_2O = 1.07, K_2O = 0.05 wt%).

Trace element abundances generally vary within the analytical error in the three sub-samples, except Cs, Rb and Ba, being much less abundant in S1 than S2 and S3 (Figure 5). Only the average values (S) are however reported in Table 2 and used for discussion. Primordial-mantle (PM) normalized compatibility diagram (Figure 5) indicates that Cs and Ba are enriched with respect to PM values (80 × PM and 45 × PM, respectively), whereas Pb is below the detection limits. In general, moderately compatible elements vary between 1 × PM and 10 × PM values. Highly compatible elements, especially Cr (= 94 ppm), are instead much lower than PM values. The CI-normalized REE variations (Figure 6) display a gently down-sloping pattern, as they vary from about 30 × C1 (La) to about 10 × CI. A slight Eu positive anomaly occurs, for example, (Eu_N/Eu*) = 1.18.

5. Discussion

Texture does not provide univocal indication on the sample origin. On the one hand, geometric relations between some clinopyroxene grains resemble an igneous "adcumulate" [58] texture (Figure 2a), as hypothesized in other Hyblean garnet-bearing xenoliths [42]. On the other hand, the random grain-size variation, even at the thin-section scale (Figure 2e,f), the poikiloblastic areas and the complex penetrative intergrowths of clinopyroxene and garnet grains (Figure 2c), can hardly reconcile with the crystallization of a cooling silicate melt.

Experimental results in the simplified CaO–MgO–Al_2O_3–SiO_2 (CMAS) system conducted by different authors over time (e.g., the review provided by Lambart et al. [59]), indicates that, at high pressure conditions (P ≥ 2 GPa), an Al-rich, Ca-Si-poor clinopyroxene first segregates from the liquid. Even though such characteristics may be compatible with the composition of the clinopyroxene from the sample (Table 1), the very low content in transition elements (Table 2), especially in chromium (Cr = 25 ppm) of aforementioned pyroxene may be inconsistent with the aforementioned viewpoint.

The (averaged) whole-rock chemistry of the sample (Tables 1 and 2), does not allow unequivocal interpretation, as well. Assuming an igneous origin of this rock, its Mg# value (=72.8) lays in

the uppermost side of the Mg# range for mantle-derived primary liquids, whereas the SiO_2/Al_2O_3 ratio (=2.59) would imply significant plagioclase accumulation [60]. A troctolite (Ca-rich plagioclase + Mg-rich olivine) composition may be consistent with aforementioned chemical parameters. The CIPW normative composition (vol%), assuming Fe^{3+}/total iron = 0.15, is in fact compatible with a troctolitic gabbro, for example, plagioclase ($An_{91.7}$) = 48.5%; olivine (Mg# 80.5) = 25.4%; diopside= 18.33%. On the other hand, an original troctolite composition would have produced a more pronounced positive Eu anomaly than the present one (Eu_N/Eu^* = 1.18), unless such a chemical feature has get lost during a subsequent geochemical resetting of the entire mineral assemblage. The chromium content (93 ppm) of the sample is also too low with respect to its high Mg# value, being even lower than the averaged Cr content (=249 ppm) of all MORB types [61].

Many trace elements, including some transition metals other than chromium, are compatible with a MORB-type composition [61,62]. Accordingly, some established geochemical proxies clearly indicate a basaltic *parentage*. For instance, the sample, as shown in Figure 8, plots in the "oceanic array," between the N-MORB and E-MORB representative points, in the Th/Yb vs. Nb/Yb diagram [63] and in the overlapping zone between the fields for ophiolite and "modern oceanic" gabbros in the Zr/Sm vs. Zr/Hf diagram [64]. It must be also noticed that the sample plots in the field of Hyblean gabbroic xenoliths in any of the aforementioned diagrams (Figure 8). Considering the Nb vs. Zr/Nb variations (Figure 8d), the sample plots in the overlapping zone between the field of Hyblean gabbroic xenoliths and the field of any types of Hyblean pyroxenite xenoliths [45] and references therein reported.

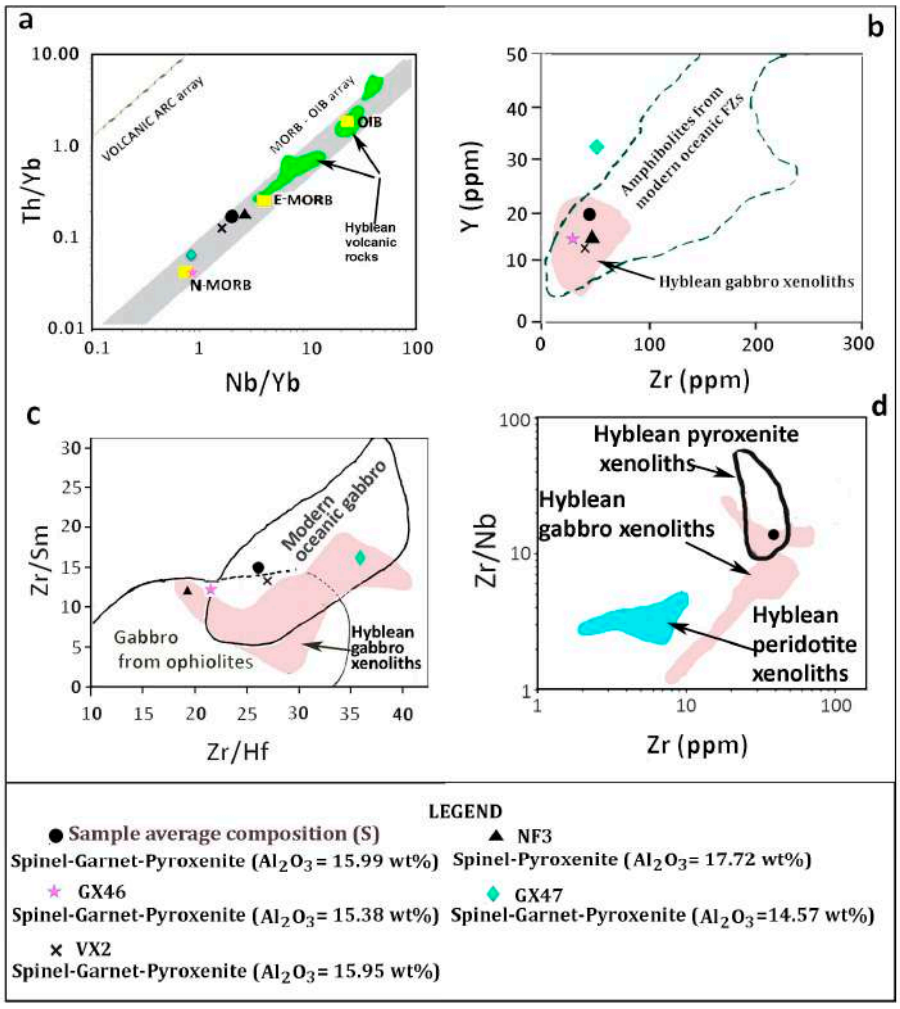

Figure 8. Variation diagrams of different trace elements and element ratios providing information on the geochemical affinity of the sample (S) and other high-Al pyroxenite xenoliths from the Hyblean

area. (**a**) Nb/Yb vs. Th/Yb diagram. The sample plots in the "oceanic array" [63]. (**b**) Zr/Y diagram. The sample plots in the field of amphibolites from modern oceanic fracture zones (FZ) [64]. Field of Hyblean gabbroic xenoliths after [17]. (**c**) Zr/Hf vs. Zr/Sm diagram. The sample plots in the overlapping zone between fields of modern oceanic gabbros and gabbros from ophiolites [64]. (**d**) Zr vs. Zr/Nb diagram. The sample plots in the overlapping area between the field of Hyblean pyroxenite xenoliths and Hyblean gabbroic xenoliths [17,45]. Sample composition: this work. High-Al pyroxenite xenolith compositions after [40,42].

The multielement diagram reported in Figure 5c indicates that some incompatible elements, especially Cs, Ba and U, are significantly enriched with respect to PM values. Such an enrichment is probably due to the modal abundance of kelyphite, which is enriched in incompatible elements, especially the fluid-mobile ones (Figure 5a). The circumstance that the "sub-sample" S1 (see previous section) has undetectable amount of Cs and lower Rb and Ba than other "sub-samples" (Figure 5c), probably depends on the heterogeneous modal distribution of garnet, hence kelyphite, in the whole rock. The chondrite-normalized REE pattern (Figure 6) is compatible with the composition of some MORB types, particularly those formed in slow-spreading settings, such as South Mid-Atlantic Ridge [62] and references therein reported.

In summary, texture, modal and chemical compositions of the sample, as well as of other Hyblean garnet-bearing pyroxenites, may lead to different, even conflicting, interpretations. The low content in Cr (and in other transition elements) and the relatively high content in incompatible elements are hardly consistent with a pyroxene accumulation from a primitive mafic magma at mantle depths.

The lack of chemical data on the rare zircon grains observed in the sample (Figure 3e,f) do not allow to get inference on their origin [65]. The optical features alone, including apparent relict cores, do not provide compelling evidence on the origin, as these can be the same for both hydrothermal [66] and igneous zircons. On the other hand, oceanic zircons, including xenocrysts, are generally considered igneous segregates [67]. Even admitting an igneous origin for the zircon grains from the sample, this fact is hardly compatible with the hypothesis that the Hyblean pyroxenites are high-pressure cumulates from a primary magma, as zircon is a typical accessory phase in highly evolved magmas. In addition, these zircon grains cannot be recycled crustal material occurring in the mantle and hence entered as xenocrysts in the crystallizing cumulus pyroxene, since zircon is highly soluble in hot mafic magma [68].

5.1. Assessing the Petrologic History of the Sample—Stage I, from Troctolitic Gabbro to Amphibolite

A MORB-type igneous protolith, probably a troctolite gabbro, may give reason to both the high Al and Mg of this rock and the distribution of several trace elements. Scientific reports of marine geology enterprises often report on troctolite bodies in different oceanic settings [69], including core complexes [70].

Although high pressure metamorphism can transform a troctolite gabbro into a garnet-pyroxenite [8], the texture of the sample is quite different from typical mafic metamorphic rocks, including eclogite. In addition, it is not clear the reason why such a relatively low density, plagioclase-rich, troctolite would have sunk in the denser mantle peridotites, at considerable depths, to undertake metamorphism. An ancient subduction process in the Hyblean region and nearby areas can be excluded on the basis of a number of independent geophysical data [13,14].

On the above grounds, it is noteworthy that the sample (average) major element distribution closely fits in a tschermakitic horneblende composition (but water), with the following mineral formula calculated on 23 oxygen-equivalent basis: $(Na_{0.296}\ K_{0.009})\ Ca_{1.939}\ Mg_{3.070}\ Mn_{0.014}\ Fe^{2+}_{0.179}\ Fe^{3+}_{0.971}\ Al_{2.685}\ Ti_{0.161}\ Si_{5.919}\ O_{22}\ (OH)_2$. The Fe^{2+}/Fe^{3+} ratio was estimated based on total cations = 13 excluding Ca, Na and K [71]. Accordingly, the modal composition of the sample is plenty compatible with the dehydroxilation reaction of the aforementioned Tschermachitic horneblende (Amph) (Reaction 1):

$$100\text{Amph} \approx 64\ \text{Cpx} + 22\ \text{Grt} + 6\ \text{Spl} + 6\ \text{Opx} + 2\ H_2O \quad (1)$$

where clinopyroxene (Cpx), spinel (Spl) and Garnet (Grt) have the same composition of the respective mineral phases in the sample (Table 1).

The consistency of the sample whole rock composition with an amphibole could be a mere fortuitous circumstance, having therefore no petrologic implications, also considering that existing amphibole types cover a wide range of compositions. On the other hand, almost each of the published chemical analyses of the Hyblean aluminous-pyroxenite xenoliths [40,42] exhibits the same intriguing resemblance to Tschermakite-rich amphiboles.

The formation of a pyroxene-rich, even garnet-bearing, dry mineral assemblage from a hydrous protolith, releasing an aqueous solution as free fluid, is an established petrologic process in a wide range of metamorphic systems, including metabasites [72]. Moreover, amphibole phenocrysts in volcanic rocks the world over display plenty evidence of breakdown reactions with pyroxene formation. For example [73] described amphibole partially replaced by pseudomorphs of augite. There are published experimental results indicating that amphibole phenocrysts, in equilibrium with magma with different compositions, give rise to calcic pyroxene as breakdown product at low-pressure, high-temperature conditions. De Angelis et al. [74] experimentally investigated the formation of reaction rims in amphibole phenocrysts. Their results indicate that heating up to 900 °C both destabilizes amphibole and also reduces melt viscosity, favoring faster reaction kinetics. Heating-induced reaction rims almost always contain both orthopyroxene and clinopyroxene ± plagioclase ± Fe-Ti oxides. Rutherford and Devine [75] investigated andesitic systems, demonstrating that horneblendite breakdowns to pyroxenite at T = 860 °C and P(H_2O) = 130 MPa. Even though the composition of the starting materials used by De Angelis et al. [74] and Rutherford and Devine [75] was quite different from the present ultramafic system, their results give useful indications. Thermodynamic model by Baxter and Caddik [76] indicates that an amphibolite, deriving from an altered (3.5 wt% H_2O) mid-oceanic-ridge basalt, can give a pyroxene- and garnet-bearing anhydrous mineral assemblage in a P–T range of 580–750 °C and 1.6 and 2.2 GPa, respectively.

Multi-stage hydration and dehydration processes at different conditions of pressure, temperature and fluid conditions have been reported in the modern oceanic lithosphere [77], especially in magma-starving and strongly fractured settings. There are numerous reports on amphibolite bodies in slow-spreading ridges, fracture zones and core-complexes, as, for example, the intersection area between the Mid-Atlantic Ridge (MAR) crest zone and the Fifteen Twenty (Cape Verde) Fracture Zone [78]. Some of these amphibolites are almost totally monomineralic (e.g., hornblendite and actinolitite [78]).

Experimental results on amphiboles related to mafic systems indicate that the Tschermak substitution, $Mg^{vi} + Si^{iv} = Al^{iv} + Al^{vi}$, is closely related to pressure increasing at constant temperature [79]. In this respect, the relatively high Al (iv) content (= 1.92 a.p.f.u.), calculated from the formula of the putative amphibole protolith, would imply high pressure conditions. At high pressure, amphibole breakdown reactions occur at vapor-absent, melt-present, conditions (dehydration melting, e.g., Wolf and Wyllie [80]). A water-undersaturated, felsitic melt would have therefore coexisted, as reaction product, with the pyroxenite restite. Evidence of felsitic melts, either as granitoid xenoliths or felsitic veins in ultramafic and mafic xenoliths, including pyroxenites, has however never found in the Hyblean area.

Even though the Tschermak substitution, as previously stated, is favored by high-pressure conditions, at a specified P and T, the Al content of calcic amphiboles, it also depends on the coexisting mineral assemblage and hence on the bulk-rock chemical composition. There are cases where a high aluminous horneblende (Al_2O_3 up to 19 wt%) is formed at pressure as low as 380 Mpa [81]. In case of amphibole formation from the reaction between plagioclase and olivine, as it occurs in troctolites, products with high Al^{iv} and Fe^{3+} are therefore expected [82].

Hydrothermal metasomatic reactions can strongly modify the composition of the oceanic crust, giving also rise to significant concentration of aluminous phases, such as Al-spinel, corundum and even diaspore [69]. Notwithstanding the very low solubility of Al in aqueous fluids, the aluminum

transport is thought to be greatly enhanced by hot, saline fluids [83]. Such halogen rich fluids are also capable to create chemical complexes with, hence transporting, HFSE elements, including Zr [84]. In cases of de-complexation in zones rich in silica, the precipitation of hydrothermal zircon is very likely [85]. Moreover Nozaka et al. [69] suggested that the hydrothermal alteration of troctolites in the deep oceanic crust induces loss of Ca^{2+} and SiO_2(aq) in high-temperature hydrothermal fluids, giving therefore rise to a passive aluminum enrichment in the related secondary minerals. In particular, aforementioned authors reported that Al-spinel + pargasite ± anorthite is the earliest stage and highest temperature alteration assemblage observed in the lower plutonic crustal section at Hess Deep (East Pacific Rise), at approximately 700 °C and a minimum pressure value of about 140 MPa.

5.2. Assessing the Petrologic History of the Sample—Stage II, from Amphibolite to Garnet–Pyroxenite

On the above grounds it seems reasonable to hypothesize that the Al-rich pyroxenite sample originated from subsolidus dehydration of an amphibolite protolith. The amphibolite perspective can be extended to all Hyblean aluminous pyroxenites. Accordingly, the Zr vs. Y ratio of the sample (Figure 8c) plots in the field of amphibolites from modern oceanic fracture zones [64]. The hypothesized amphibolite body was the consequence of the hydrothermal metasomatism of a troctolitic gabbro, likely intruded into the already exhumed mantle peridotites or during the exhumation event. Some geochemical parameters of the sample, such as the Th/Yb vs. Nb/Yb and Zr/Sm vs. Zr/Hf plots (Figure 8), compatible with MORB values, were likely inherited from the troctolitic gabbro ancestor.

The amphibolite dehydration was probably due to the transient temperature increasing nearby the contact with a basaltic magma intrusion, very likely in form of a dike swarm. The thermal condition at the contact aureole depends on several parameters, such as the dike thickness; intrusion temperature; host-rock temperature and pressure (depth) conditions, persistence of the event over time and so forth. Numerical modeling by Aarnes et al. [86] considers a basaltic sill, 100 m in width, 800 m in length, with an initial temperature of 1150 °C, intruded in country rocks at a temperature of 100 °C. The authors calculated that in 100 years a thermal aureole about 200 m in thickness, with an average temperature of 650 °C, can be formed. Considering instead a dyke swarm intruding an amphybolite section of about 1 km in width, with a basalt temperature of about 1100 °C, it is very likely that in the inner area of the dyke swarm temperature can reach values as high as 800–900 °C. In this respect, Leeman et al. [87] suggested that in case of a dike/sill swarm intrusion overall reaching several kilometers in thickness, hence closely repeated over time in the same zone, temperature of the entire area can reach values high enough to induce significant melting in the felsitic sedimentary country rocks.

The coarse grain of the Hyblean pyroxenite may be a primary feature, as the aqueous fluids released by the amphibole protolith catalyzed the growth of the crystals, fluxing eventually out the system through an adequate fracture network. In addition, these fluxing aqueous fluids have had the important role to inhibit the plagioclase nucleation [88]. On the other hand, it is also possible, even likely, that the original texture and mineral composition of the anhydrous reaction products were modified by subsequent recrystallization under different P-T conditions.

Garnet can be one of the products of the breakdown of an amphibole-rich protolith, both in sub-solidus and supra-solidus conditions [76]. As previously mentioned, an amphybolite dehydration melting is not probable in the study case. More importantly, textural relationships between spinel and garnet, as described in the relevant section, may suggest that garnet has grown at the expense of Al-spinel and clinopyroxene. It is therefore reasonable to consider a two-steps process, as first amphibole broke-down to an Al-rich clinopyroxene and Al-spinel (± Ca-poor, Al-rich pyroxene). In response to an increasing pressure and/or decreasing temperature conditions, clinopyroxene reacted with spinel to give rise to garnet, as experimental results by Herzberg [5] suggest. In addition, texture relationships between Ca-rich and Ca-poor pyroxenes observed in the sample indicate that part, if not all, of the Ca-poor pyroxene ex-solved from the clinopyroxene in a later stage, as a probable consequence of a further temperature decreasing of the system.

Considering a magma-starving ridge as a likely geological context for Hyblean garnet-pyroxenite formation, time interval between two igneous episodes is there long enough to give rise to a significant temperature decreasing of the lithosphere at regional scale. It is therefore most probably that the garnet-forming reaction was due to temperature decreasing. The re-equilibration event involved, of course, the entire mineral assemblage and a general recrystallization of the rock therefore occurred. The "X-shaped" REE patterns of garnet and clinopyroxene in the sample, as shown in Figure 6, in fact indicates the coeval formation of aforementioned mineral phases, at near-chemical equilibrium conditions. Accordingly, no textural evidence of reaction relationships between clinopyroxene and garnet (now kelyphite) appears in the sample, except cases where fluids channelized through microfractures induces coarsening of the kelyphite grain-size (Figure 2d).

5.3. Assessing the Petrologic History of the Sample—Stage III, Kelyphite Replaces Garnet

Kelyphite, which replaces wide areas of the garnet, testifies that further changes occurred in thermodynamic parameters of the system. The kelyphite mineral assemblage, which includes plagioclase, even though widely replaced by alteration products, is, in the bulk, less dense than the original garnet, indicating that a decompression event occurred during the geological history of the sample. Decompression can be either associated to a slowly developing geological event, such as a regional lithosphere uplifting or a sudden upwelling of the sample, likely associated to its eruptive history as xenolith entered in the upwelling diatreme system. Considering that the uprising of a fluidized igneous system through the diatreme pipe is a very fast event [89], the kelyphite formation seems therefore improbable, as decompression melting or permanence of metastable garnet should be kinetically more favored than subsolidus recrystallization process in such explosive eruption [90]. The regional sedimentary sequence, as depicted by drill-cores and field evidence, indicates that a tectonic uplifting of this region occurred since the Early Cretaceous. A slow decompression during regional uplifting is therefore the most probable cause for kelyphite formation. Volatiles certainly played an important role in the local recrystallization and grain-size coarsening of the kelyphite.

As already mentioned, the kelyphite bulk composition closely matches the original garnet but lower calcium and higher incompatible element amounts. This circumstance is probably related to the replacement of the kelyphite plagioclase by hydrous alteration products (e.g., chlorite). Such a hypothesis is consistent with the strong negative Eu anomaly (e.g., Eu/Eu * = 0.28) depicted by the kelyphite REE patterns (Figure 6), which may suggest that previous plagioclase has been removed. The fluid(s) related to such an alteration, percolating through the finely porous kelyphite, has taken out calcium and released some highly incompatible elements, such as Li, Cs, Rb, Ba, U.

5.4. Further Discussion

Isotope geochemistry on Hyblean pyroxenite xenoliths (all types), as can be seen from the literature, may give useful information. For instance, the $^{143}Nd/^{144}Nd$ ratio is in the range 0.51290–0.5130 [24,44,45], closely overlapping to the range recorded in Hyblean gabbroic xenoliths [91]. Helium isotope ratios were also detected in some pyroxenite xenoliths [45]. In particular, $^{3}He/^{4}He$ were measured in CO_2-dominated fluid inclusions in clinopyroxene grains, indicating MORB-type values (e.g., Ra = 7.1–7.6, where Ra is the $^{3}He/^{4}He$ ratio of 1.38×10^{-6} as measured in air). Accepting, for instance, the pyroxenite formation mechanism put forward in the present paper, it may be suggested that He (as well as CO_2 and other mantle-derived gases) trapped in these pyroxene grains derived from the degassing of the basalt magma intruded in the amphibolite and hence responsible for pyrometamorphism and amphibole breakdown. Conversely, it seems unlikely that such gases were inherited from the troctolitic gabbro ancestor, since the hydrothermal process that transformed the troctolite into amphibolite would have caused a general isotopic resetting.

The sample modal mineralogy, consisting of two-pyroxenes, spinel and garnet, may induce to estimate equilibration P-T values by established mineralogical geothermobarometers. On the other hand, if we accept the hypothesis put forward in this paper, the phase chemistry of the sample is

strongly controlled by the chemical composition of the Al-amphibolite protolith rather than by the P-T conditions [81]. This fact and the evidence of local disequilibrium conditions (e.g., the exsolution of Ca-poor pyroxene from the calcic one and the kelyphite after garnet), unfortunately make impractical the use of geothermobarometers.

6. General Implications: Gravity Instability Development and the "Autochthonous-Recycled" Nature of Intraplate Garnet–Pyroxenites

Aforementioned discussion bears some implications which extend beyond the regional limits. These general implications are briefly reported below, since an exhaustive discussion would require a multidisciplinary approach, especially in the fields of geophysics, structural geology and petrophysics.

6.1. Convective Instability in the Oceanic Lithosphere—The Garnet-Pyroxenite Perspective

Density (ρ) measures on Hyblean spinel-pyroxenite (± garnet, ± plagioclase) xenoliths at room pressure and temperature conditions, gave values in the range 3290–3380 kg m^{-3} [92,93]. The measured density of the sample (ρ = 3377 kg m^{-3}) fits in the aforementioned range. In addition, density measures on a set of peridotite samples, consisting of spinel-harzburgites with serpentinization (±carbonation) degree between 5 and 12% by volume, are in the range 2960–3320 kg m^{-3} [92,93]. Measured density values in xenoliths are certainly lower than those of the same rocks set in their original deep-seated contexts, due, for example, to pore closure. Considering that this circumstance is equally true for both pyroxenites and peridotites, the density contrast (Δρ) between the aforementioned rock types remain unaffected. Exhumed mantle peridotites in oceanic fracture zones usually undergo serpentinization, which strongly affects their density values [94,95]. On these grounds, the density contrast between "dry" garnet-pyroxenites and "wet" peridotites with 10–100% serpentinization, can be estimated in the range 150–400 kg m^{-3}.

Jull and Kelemen [96] reported that a density contrast between the lowermost lithosphere and the underlying asthenosphere as low as 50 kg m^{-3} is sufficient to trigger "convective instability" that is, the denser material sinks under the action of gravity, while the lighter one, behaving like a fluid, rises to take its place. Gradients of the gravity acceleration due to density contrast, however, may be not sufficient to give rise to departures from metastable hydrostatic equilibrium, as they can be damped, for instance, by the viscosity of the lighter medium [97]. Moreover, viscosity, as known, is closely related to composition, temperature and stress conditions of the system (e.g., strain rate proportional to deviatoric stress, raised to a power n [98]), as can be seen from the classic works by Rayleigh [99] and Taylor [100] (e.g., "Rayleigh–Taylor instability" [98]).

Pressure is also an important factor controlling the convective instability, as it affects the subsolidus phase equilibria, hence the densities, of the rock-forming minerals. Jull and Kelemen [96] calculated that geotherms of 800 °C and 1000 °C favor convective instability for rocks where garnet formation occurs on increasing pressure conditions. On the contrary, high temperature reduces densities of mafic and ultramafic rocks where garnet never forms, hampering therefore instability conditions. Convective instability at the lithosphere—asthenosphere boundary is a slowly developing process over geological time. Such a process is strongly favored by lateral heterogeneity and transient temperature variations [98].

In cases where convective instability is attained, the descending velocity of the heavy body is a crucial parameter to consider, which is closely related to the size of the involved heavy body. Brueckner [101] calculated, on the basis of the Stokes' formula, that a sphere of a heavy material with a 500 m diameter can sink in a lighter material with a viscosity of 10^{20} kg $m^{-1}s^{-1}$ over 1 km in 20 MA, provided a constant density contrast of 300 kg m^{-3}. A smaller sphere, 12 m in diameter, can instead sink at the same velocity (1 km in 20 MA) only in case of higher density contrast (e.g., 500 kg m^{-3}) and lower viscosity of the country rocks (e.g., 10^{17} kg m^{-1} s^{-1}). Even though these absolute velocity values are roughly indicative due to the significant simplifications imposed by the model, the relationships between the body size and its descending velocity is unequivocal.

Garnet pyroxenite lenses, a few tens of meters in length, a few tens of centimeters in width, with a density contrast to their country rocks $\Delta\rho \leq 300$ kg m^{-3}, can indefinitely rest in metastable gravitational equilibrium, their presence being therefore neutral with respect to regional tectonic processes. Such a scenery fits in the aforementioned results regarding the Hyblean pyroxenites, since the kelyphitic breakdown of the garnet suggests that garnet pyroxenites were passively included in the final plateau uplift, notwithstanding the negative buoyancy gradient. On the contrary, there may be different cases in which large volumes (up to several cubic kilometers) of (pyrometamorphic?) garnet–pyroxenites can be form in the lower oceanic lithosphere, apt to induce convective instability.

Numerical models addressing geological cases of Rayleigh–Taylor instability, such as the case of convective thinning of the continental lithosphere (e.g., Houseman and Molnar [98]), are hardly consistent with oceanic slow-spreading ridges or fracture zones, where the crust is virtually lacking and hence the lithospheric mantle is tectonically exhumed at seafloor [102–105]. In such oceanic contexts, the serpentinization process can involve sections of the exhumed mantle up to 25 km in thickness [105]. It is therefore expected that in these zones the lithosphere must be mechanically weak, with a semi-ductile behavior, even at a few kilometers beneath seafloor, as the addition of water to nominally anhydrous minerals dramatically decreases their viscosity [106,107]. On the contrary, in continental settings, where the lithosphere viscosity depends primarily on temperature, a viscosity of about 10^{17} kg m^{-1} s^{-1}, consistent with convective instability, is thought to occur at a depth $\geq$ 50 km [98]. Moreover, models considering horizontally extended layers, such as those related to the lower continental lithosphere, do not fit in geological contexts dominated by a sub-vertical fracture system, which drives seawater penetration and hence serpentinization [104,105] as well as hydrothermal circulation and even magma upwelling. The vertical fracture systems also probably controls the shape of igneous intrusive bodies and hence the shape of the geological bodies produced by pyrometamorphism, such as the aforementioned garnet pyroxenite lumps (Figure 9).

A system consisting of a vertically elongated body of heavy garnet-pyroxenites, a few cubic kilometers in size, with an average density of ~3370 kg m^{-3}, immersed in a large volume of widely serpentinized, mantle peridotites, with an average density of ~3000 kg m^{-3} [108] ($\Delta\rho$~370 kg m^{-3}), is characterized by gravitational gradients which likely induce anisotropic stress field in the system. As in any displacements of a finite body in a medium, shear deformation occurs along its boundaries [109]. There porosity and permeability should increase and hence water, deriving from local serpentinite dehydroxilization, will decrease the shear resistance to nearly zero [110]. The gravity force therefore exceeds the shearing resistance to frictional sliding and hence the pyroxenite body can start moving downward. Shear would be irregularly distributed along the ductile sliding surfaces, possibly causing the pyroxenite body to be deformed into different shapes [101]. In this stage of the process, the room left free on top of the sinking body may be partially replaced by the overlying serpentinites which collapse through a fault system, giving therefore rise to the basin deepening [111] and a possible formation of a trench structure. Aforementioned concepts are artistically depicted in Figure 9.

Going into more detail, responses of low-porosity, hydrous rocks such as serpentinites, to mechanical loads, are porosity generation via microcracking, frictional heating generation, dehydration embrittlement, brittle faulting. The descending motion of the pyroxenite body through the serpentinized peridotites therefore induces frictional heating, local dehydration, brittle fracturing and permeability enhancement [112], with a significant reduction in the rock strength [113]. Lateral creeping can therefore occur with final accumulation of "sheared" [114] or "muddled" serpentinite masses at the bottom-edges of the sinking pyroxenite body. Such a muddled serpentines, being less dense than the overburden, can up well as a diapir to shallow levels [115], eventually going to occupy the space left empty by the sinking body, for example, shallow-seated convective instability is attained.

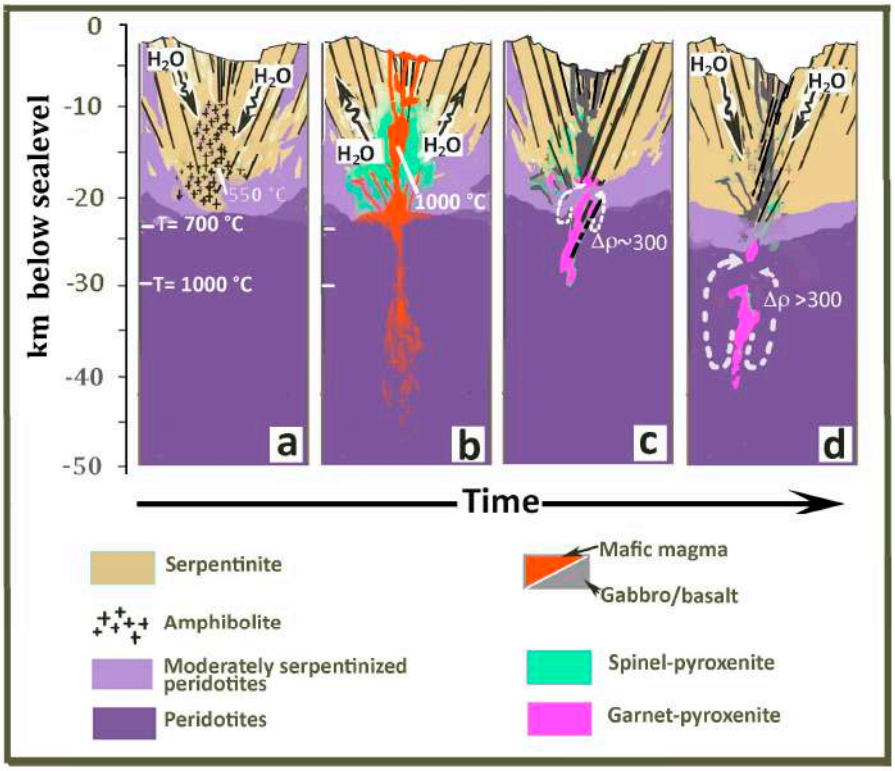

Figure 9. Cartoon showing a possible sequence of events, over undefined time (several Ma), in an imaginary ultra-slow spreading ridge geological section (not to scale). The basic context was roughly derived from [105]. The storyline stems from the results of the present paper. (**a**) An Al-rich amphibolite body, derived from the hydrothermal alteration of a troctolitic gabbro, is set in fractured serpentinite country rocks. (**b**) A transient increasing in temperature, due to an igneous intrusion, induces diffuse dehydroxylization and spinel-pyroxenite formation. (**c**) Re-equilibration of the spinel-pyroxenite minerals due to isobaric cooling induces garnet-growth and positive density contrast with the country rocks. Adequate rheological conditions give eventually rise to convective instability and (**d**) sinking of a large garnet-pyroxenite lump in the ductile mantle.

If the descending motion of the pyroxenite body will continue until the depth corresponding to the 700 °C isotherm is reached, the density contrast due to the occurrence of serpentine minerals in the country rocks will vanish, as these are far out their stability fields [109]. Temperature therefore turns to be the most important parameters that controls the density of materials. In this respect, it is reported that the density of Mg-rich olivine will decrease of about 3% at 1000 °C [89]. Such a minor density decreasing is thought to be sufficient to drive mantle convective motions at planetary scale [96]. Considering the relatively high pressure associated to such high temperatures, the garnet should remain as an equilibrium phase. A positive density contrast between garnet-pyroxenites and mantle peridotites therefore remains and the descending motion of the garnet pyroxenite body continues even at a faster rate, as the viscosity of the country rocks is further decreasing. Variable amounts of partial melting, with mafic composition, is however expected in the garnet pyroxenite, due to the low melting point of Al-rich pyroxenes [38]. The newly formed melt will decrease the density contrast, as it decreases the density of the pyroxenite. The descending motion will definitively stop when a neutral buoyancy is reached.

A further speculation is about the possibility that more or less large portions of serpentinized peridotite country rocks remain attached to the walls of the sinking pyroxenite body, being therefore passively involved in the descending motion. Dehydration or dehydration-melting reactions will therefore occur when the descending rocks will reach loci of thermodynamic instability of the related hydrous minerals. The embrittlement consequent to dehydration gives likely rise to seismic activity, as

fluids increase the pore pressure of the country rocks, hence reduces normal stress across potential planes of weakness, in a part of the system where high pressure and temperature conditions would normally prohibit earthquake rupture [109]. In addition, the released fluids may induce partial melting in the surrounding mantle peridotites. This looks like a slab-related scenery, especially in cases where oceanic slabs are gravitationally sinking [116,117].

6.2. The Garnet Geochemical Signature in Oceanic Basalts—The "Recycled-Autochthonous Pyroxenite" Hypothesis

Descending lumps of garnet-pyroxenites, as above described, can therefore be efficient metasomatic agents of the sub-oceanic mantle. Different amounts of pyroxenites, including garnet-bearing types, are thought to occur in the convective peridotitic mantle, in order to give reason to the geochemical and isotopic characteristics of mantle-derived magmas in different geological contexts worldwide, including oceanic ridge segments [10,118].

For example, Lambart et al. [59] envisaged the chemical signature of a silica-deficient pyroxenite in basaltic glasses with MgO ~9 wt% having both a higher FeO content and a lower SiO_2 content than the usual primitive MORBs. Regarding trace elements distribution, Hirschmann and Stolper [119] highlighted that Sm/Yb ratios of average MORB from regions of typical crustal thickness are difficult to reconcile with derivation by melting of spinel peridotite only but can be explained if MORB sources contain ~5% garnet pyroxenite. Accordingly, Saccani et al. [118] suggested that basalts characterized by significant depletion in heavy REE (HREE) with respect to medium REE (MREE) derive from a depleted mantle source characterized by garnet-bearing mafic layers. More precisely, aforementioned basalts are indicated as G-MORBs, where "G" stands for garnet, being discriminated from other MORB-types by Th–Nb and Ce–Dy–Yb systematics [118]. Occurrence of 3%–6% pyroxenite with ≥20% modal garnet also gives reason to some isotopic characteristics of MORBs, such as the Lu–Hf and Sm–Nd systematics and the $(^{230}Th)/(^{238}U)$ abundances [118].

Such garnet pyroxenites in the mantle source of MORBs are either considered autochthonous products of the crystallization of partial melts at mantle depths [4,11] or "recycled" products, related to subducting slabs of oceanic crust at convergent plate margins [7,10]. As mentioned in the introductive section, in the first case, an auto-metasomatism due to cognate cumulates can hardly confer exotic geochemical and isotopic signatures to partial melts from the same mantle source. In the latter case, it seems unlikely that recycled material can be passively transported in the convective mantle with no severe melting and/or isotopic equilibration with the host mantle rocks.

The shallow (crustal) origin of garnet-pyroxenites in amagmatic oceanic ridges and fracture zones and the consequent convective instability development, as above reported, may give reason to the presence of such "recycled" rocks even in areas very distant from collisional structures. In this respect, it must be highlighted that the chemical composition of such "recycled-autochthonous" pyroxenites, which derive from an amphibolite protolith, can have various chemical compositions, due, for example, to the presence/lack of particular mineral phases, such as feldspar, in the modal assemblage of the parent amphibolite. This circumstance may explain the occurrence of different geochemical and isotopic signatures of recycled crustal components in oceanic basalts [120], either MORBs or OIBs.

7. Conclusions

The results of the present study suggest that the Hyblean Al-rich pyroxenites were formed by subsolidus dehydration of Al-rich oceanic amphibolites, at high-temperature (700–900 °C) and relatively low-pressure conditions (0.3–0.8 GPa), nearby the contact surfaces with upwelling basalt magma. The Al-rich amphibolites derived from the hydrothermal metasomatism of a troctolitic gabbro ancestor in a magma-starving oceanic ridge or core-complex. An Al-spinel pyroxenite was the first product of aforementioned breakdown process. The subsequent isobaric cooling of the system induced the garnet-forming reaction between Al-spinel and clinopyroxene.

The presumably small size of the Hyblean garnet-pyroxenite masses let them to rest in metastable equilibrium conditions in the lighter serpentinite country rocks, despite of the occurrence of a negative buoyancy gradient. The late tectonic uplift of the Hyblean Plateau gave rise to partial breakdown of garnet to kelyphite. The high aluminum content in the pyroxenite mineral phases depends on the chemical composition of the original amphibolite and hence on the composition of the troctolitic gabbro ancestor, having no relationships with the pressure conditions.

Such results also put forward some implications of general interest, briefly mentioned in the paper, as an exhaustive discussion could only be carried out on a multidisciplinary basis. For instance, the positive density contrast between the garnet-bearing pyroxenites and their peridotite country-rocks can be sufficient to induce convective instability, provided favorable viscosity parameters and an adequate size of the descending geological bodies. Such favorable conditions can both occur in the exhumed, serpentinized section of the mantle and in its deep-seated, hot, ductile section, hence providing an explanation to the occurrence of "recycled" crustal material in zones of the subocenic mantle far away from subduction centers. If the descending garnet pyroxenites are involved, together with the host spinel-peridotites, in partial-melting events, they can impart the related basaltic melts the well-known “garnet geochemical signature.”

This work poses the following question, addressed mostly to geophysicists, whether or not descending swarms of garnet-pyroxenite blocks, detached from a ridge axial zone, can originate in the oceanic mantle favorable rheological conditions (e.g., a low-viscosity channel) for the detachment and sinking of large slabs of brittle lithosphere even without initial density contrast. This fact, if proved, may be useful to explain some atypical intraoceanic subduction events [117,121]. On the other hand, the results reported here do not question established viewpoints on plate tectonics [122], as only specific geological cases are here addressed, mostly related to oceanic contexts, where expansive serpentinization [102–105] can modify the rheological characteristics [94,106] of large section of the lithosphere.

Author Contributions: V.S. conceived and wrote the paper. S.C. reviewed the geological aspects. Both authors contributed to the evaluation and discussion of the data. All authors have read and agreed to the published version of the manuscript.

Funding: Universitaà di Catania, Piano per la ricerca 2016–2018, II annualitaà (to S.C.).

Acknowledgments: We acknowledge many thanks to Alessandra Correale (INGV, Palermo), for having performed the Laser Ablation analyses and to Germana Barone and Paolo Mazzoleni (University of Catania), for having provided the micro-Raman spectra discussed in this paper. We greatly appreciate the constructive comments by two anonymous Reviewers.

Conflicts of Interest: The author declares that there are no conflicts of interest, nor other ethical issues, concerning this work.

References

1. Downes, H. Origin and significance of spinel and garnet pyroxenites in the shal-low lithospheric mantle: Ultramafic massifs in orogenic belts in Western Europe and NW Africa. *Lithos* **2007**, *99*, 1–24. [CrossRef]
2. Liu, T.-C.; Presnall, D.C. Liquidus Phase Relations in the System CaO–MgO–Al_2O_3–SiO_2 at 2 0 GPa: Applications to Basalt Fractionation, Eclogites and Igneous Sapphirine. *J. Petrol.* **2000**, *41*, 3–20. [CrossRef]
3. Berger, J.; Féménias, O.; Coussaert, N.; Demaiffe, D. Magmatic garnet-bearing mafic xenoliths (Puy Beaunit, French Massif Central): P–T path from crystallization to exhumation. *Eur. J. Mineral.* **2005**, *17*, 687–701. [CrossRef]
4. Keshav, S.; Sen, G.; Presnall, D.C. Garnet-Bearing xenoliths from Salt Lake Crater, Ohau, Hawaii: High-Pressure Fractionational Crystallization in the Oceanic mantle. *J. Petrol.* **2007**, *48*, 1681–1724. [CrossRef]
5. Herzberg, C. Pyroxene geothermometry and geobarometry: Experimental and thermodynamic evaluation of some subsolidus phase relations involving clinopyroxene in the system CaO–MgO–Al_2O_3–SiO_2. *Geochim. Cosmochim. Acta* **1978**, *42*, 945–957. [CrossRef]

6. Berger, J.; Caby, R.; Liégeois, J.-P.C.; Mercier, J.-C.C.; Demaiffe, D. Dehydration, melting and related garnet growth in the deep root of the Amalaoulaou Neoproterozoic magmatic arc (Gourma, NE Mali). *Geol. Mag.* **2008**, *146*, 173–186. [CrossRef]
7. Day, J.M.D.; Pearson, D.G.; Macpherson, C.G.; Lowry, D.; Carracedo, J.-C. Pyroxenite-Rich mantle formed by recycled oceanic lithosphere: Oxygen–Osmium isotope evidence from Canary Island lavas. *Geology* **2009**, *37*, 555–558. [CrossRef]
8. Godard, G. Eclogites and their geodynamic interpretation: A. history. *J. Geodyn.* **2001**, *32*, 165–203. [CrossRef]
9. Morten, L.; Obata, M. Possible high-temperature origin of pyroxenite lenses within garnet peridotite, northern Italy. *Bull. Mineral.* **1983**, *106*, 775–780. [CrossRef]
10. Brunelli, D.; Cipriani, A.; Bonatti, E. Thermal effects of pyroxenites on mantle melting below mid-ocean ridges. *Nat. Geosci.* **2018**. [CrossRef]
11. Dantas, C.; Ceuleneer, G.; Python, M.; Freydier, R.J.; Warren, R.J.; Dick, J.B. Pyroxenites from the Southwest Indian Ridge, 9–16°E: Cumulates from Incremental Melt Fractions Produced at the Top of a Cold Melting Regime. *J. Petrol.* **2007**, *48*, 647–660. [CrossRef]
12. Bianchi, F.; Carbone, S.; Grasso, M.; Invernizzi, G.; Lentini, F.; Longaretti, G.; Merlini, S.; Mostardini, F. Sicilia orientale: Profilo geologico Nebrodi-Iblei. *Mem. Soc. Geol. Ital.* **1987**, *38*, 429–458.
13. Giampiccolo, E.; Brancato, A.; Manuella, F.C.; Carbone, S.; Gresta, S.; Scribano, V. New evidence for the serpentinization of the Palaeozoic basement of southeastern Sicily from joint 3-D seismic velocity and attenuation tomography. *Geophys. J. Int.* **2017**, *211*, 1375–1395. [CrossRef]
14. Musumeci, C.; Scarfì, L.; Palano, M.; Patanè, D. Foreland segmentation along an active convergent margin: New constraints in southeastern Sicily (Italy) from seismic and geodetic observations. *Tectonophysics* **2014**, *630*, 137–149. [CrossRef]
15. Vai, G.B. Development of the palaeogeography of Pangaea from Late Carboniferous to Early Permian. *Palaeogeogr. Palaeoclimatol. Palaeoecol.* **2003**, *196*, 125–155. [CrossRef]
16. Scribano, V. The ultramafic and mafic nodule suite in a tuff-breccia pipe from Cozzo Molino (Hyblean Plateau, SE Sicily). *Rend. Soc. Ital. Mineral. Petrol.* **1987**, *42*, 203–217.
17. Scribano, V.; Sapienza, G.T.; Braga, R.; Morten, L. Gabbroic xenoliths in tuff-breccia pipes from the Hyblean Plateau: Insights into the nature and composition of the lower crust underneath Southeastern Sicily, Italy. *Mineral. Petrol.* **2006**, *86*, 63–88. [CrossRef]
18. Natland, J.H.; Dick, H.J.B. Formation of the lower ocean crust and the crystallization of gabbroic cumulates at a very slowly spreading ridge. *J. Volcanol. Geotherm. Res.* **2001**, *110*, 191–233. [CrossRef]
19. Scribano, V.; Ioppolo, S.; Censi, P. Chlorite/smectite-alkali feldspar metasomatic xenoliths from Hyblean Miocenic diatremes (Sicily, Italy): Evidence for early interaction between hydrothermal brines and ultramafic/mafic rocks at crustal levels. *Ofioliti* **2006**, *31*, 161–171.
20. Manuella, F.C.; Scribano, V.; Carbone, S.; Brancato, A. The Hyblean xenolith suite (Sicily): An unexpected legacy of the Ionian–Tethys realm. *Int. J. Earth Sci.* **2015**, *104*, 1317–1336. [CrossRef]
21. Manuella, F.C.; Scribano, V.; Carbone, S.; Brancato, A. Reply to "Comment on Manuella et al 'The Hyblean xenolith suite (Sicily): An unexpected legacy of the Ionian–Tethys realm' by Beccaluva et al 2015". *Int. J. Earth Sci.* **2015**, *104*, 1685–1691. [CrossRef]
22. Longaretti, G.; Rocchi, S. Il magmatismo dell'avampaese ibleo (Sicilia orientale) tra il Trias e il Quaternario: Dati stratigrafici e petrologici del sottosuolo. *Mem. Soc. Geol. Ital.* **1990**, *45*, 911–925.
23. Carbone, S.; Grasso, M.; Lentini, F. Considerazioni sull'evoluzione geodinamica della Sicilia Sud-Orientale dal Cretaceo al Quaternario. *Mem. Soc. Geol. Ital.* **1982**, *24*, 362–386. (In Italian)
24. Tonarini, S.; D'Orazio, M.; Armenti, P.; Innocenti, F.; Scribano, V. Geochemical features of Eastern Sicily lithosphere as probed by Hyblean xenoliths and lavas. *Eur. J. Mineral.* **1996**, *8*, 1153–1173. [CrossRef]
25. Schmincke, H.-U.; Behncke, B.; Grasso, M.; Raffi, S. Evolution of the northwestern Iblean Mountains, Sicily: Uplift, Plicocene/Pleistocene sea-level changes, paleoenvironment and volcanism. *Geol. Rundsch.* **1997**, *86*, 637–669. [CrossRef]
26. Beccaluva, L.; Siena, F.; Coltorti, M.; Di Grande, A.; Giudice, A.L.; Macciotta, G.; Tassinari, R.; Vaccaro, C. Nephelinitic to tholeiitic magma generation in a transtensional tectonic setting: An integrated model for the Iblean volcanism, Sicily. *J. Petrol.* **1998**, *39*, 1547–1576. [CrossRef]

27. Trua, T.; Esperança, S.; Mazzuoli, R. The evolution of the lithospheric mantle along the N. African Plate: Geochemical and isotopical evidence from the tholeiitic and alkaline volcanic rocks of the Hyblean Plateau, Italy. *Contrib. Mineral. Petrol.* **1998**, *131*, 307–322. [CrossRef]
28. Bianchini, G.; Bell, K.; Vaccaro, C. Mantle sources of the Cenozoic Iblean volcanism (SE Sicily, Italy): Sr–Nd–Pb isotopic constraints. *Mineral. Petrol.* **1999**, *67*, 213–222. [CrossRef]
29. Correale, A.; Martelli, M.; Paonita, A.; Scribano, V.; Arienzo, I. A combined study of noble gases trace elements and Sr–Nd isotopes for alkaline and tholeiitic lava from the Hyblean Plateau (Italy). *Lithos* **2018**, *314*, 59–70. [CrossRef]
30. Carbone, S.; Lentini, F. Caratteri deposizionali delle vulcaniti del Miocene superiore negli Iblei (Sicilia Sud-Orientale). *Geol. Rom.* **1981**, *20*, 79–101.
31. Suiting, I.; Schmincke, H.-U. Internal vs. external forcing in shallow marine diatreme formation: A case study from the Iblean Mountains (SE-Sicily Central Mediterranean). *J. Volcanol. Geotherm. Res.* **2009**, *186*, 361–378. [CrossRef]
32. Scribano, V. Deep-Seated xenoliths in alkaline volcanic rocks from the Hyblean Plateau (Sicily). *Mem. Soc. Geol. Ital.* **1987**, *38*, 475–482.
33. Sapienza, G.; Scribano, V. Distribution and representative whole-rock chemistry of deep-seated xenoliths from the Iblean Plateau, southeastern Sicily, Italy. *Period. Mineral.* **2000**, *69*, 185–204.
34. Scribano, V.; Carbone, S.; Manuella, F.C. Diatreme eruption probably related to explosive interaction of rising magma with serpentinite diapirs in the shallow crust (Carlentini Formation, Hyblean area, Sicily): A xenolith perspective. *Epitome* **2007**, *2*, 130–131.
35. Manuella, F.C.; Carbone, S.; Ferlito, C.; Hovland, M. Magma–Serpentinite interaction as the origin of diatremes: A case study from the Hyblean Plateau (southeastern Sicily). *Int. J. Earth Sci.* **2016**, *105*, 1371–1385. [CrossRef]
36. Correale, A.; Scribano, V.; Paonita, A. A Volcanological Paradox in a Thin-Section: Large Explosive Eruptions of High-Mg Magmas Explained Through a Vein of Silicate Glass in a Serpentinized Peridotite Xenolith (Hyblean Area, Sicily). *Geosciences* **2019**, *9*, 150. [CrossRef]
37. Scribano, V. Origin of websterite nodules from some alkaline volcanic rocks of Hyblean Plateau (South Eastern Sicily). *Period. Mineral.* **1987**, *56*, 51–69.
38. Wilshire, E.; Shervais, J.W. Al-Augite and Cr-Diopside Ultramafic Xenoliths in Basaltic Rocks from Western United States. *Phys. Chem. Earth* **1975**, *9*, 257–272. [CrossRef]
39. Nimis, P.; Vannucci, R. An ion microprobe study of clinopyroxenes in websteritic and megacryst:ic xenoliths from Hyblean Plateau (SE Sicily, Italy): Constraints on HFSE/REE/Sr frac-tionation at mantle depth. *Chem. Geol.* **1995**, *124*, 185–197. [CrossRef]
40. Punturo, R.; Scribano, V. Dati geochimici e petrografici su xenoliti di clinopirossenite a grana ultragrossa e e websteriti nelle vulcanoclastiti mioceniche dell'alta Valle Guffari (Monti Iblei, Sicilia). *Miner. Petrogr. Acta* **1997**, *40*, 95–116. (in Italian).
41. Nimis, P. Clinopyroxene geobarometry of pyroxenitic xenoliths from Hyblean Plateau (SE Sicily, Italy). *Eur. J. Mineral.* **1998**, *10*, 521–534. [CrossRef]
42. Atzori, P.; Mazzoleni, P.; Punturo, R.; Scribano, V. Gamet-Spinel-Pyroxenite xenoliths from Iblean Plateau (South-eastern Sicily, Italy). *Mineral. Petrol.* **1999**, *66*, 215–226. [CrossRef]
43. Simakov, S.K.; Sapienza, G.; Scribano, V. Application of a recent garnet-clinopyroxene geobarometer to mantle-pyroxenite xenoliths from Hyblean Plateau, south-eastern Sicily, Italy. *GeoActa* **2001**, *1*, 91–95.
44. Bianchini, G.; Yoshikawa, M.; Sapienza, G.T. Comparative study of ultramafic xe-noliths and associated lavas from South-Eastern Sicily: Nature of the lithospheric mantle and insights on magma genesis. *Mineral. Petrol.* **2010**, *98*, 111–121. [CrossRef]
45. Correale, A.; Martelli, M.; Paonita, A.; Rizzo, A.; Brusca, L.; Scribano, V. New evidences of mantle heterogeneity beneath the Hyblean Plateau (southeast Sicily, Italy) as inferred from noble gases and geochemistry of ultramafic xenoliths. *Lithos* **2012**, *132*, 70–81. [CrossRef]
46. Morimoto, N.; Fabries, J.; Ferguson, A.K.; Ginzburg, I.V.; Ross, M.; Seifert, F.A.; Aoki, K.; Gottardi, G. Nomenclature of Pyroxenes. *Min. Petr.* **1988**, *39*, 55–76. [CrossRef]
47. Papike, J.J.; Cameron, K.; Baldwin, K. Amphiboles and pyroxenes: Characterization of other than quadrilateral components and estimates of ferric iron from microprobe data. *Geol. Soc. Am. Abstr.* **1974**, *6*, 1053–1064.

48. Palme, H.; O'Neill, H.S.C. Cosmochemical estimates of Mantle Composition. In *Treatise on Geochemistry*; Holland, H.D., Turrekian, K.K., Eds.; Elsevier: Amsterdam, The Netherland, 2004; pp. 1–38.
49. Mcdonough, W.F.; Sun, S.S. The Composition of the Earth. *Chem. Geol.* **1995**, *120*, 223–253. [CrossRef]
50. Kolesov, B.A.; Geiger, C.A. Raman spectra of silicate garnets. *Phys. Chem. Miner.* **1998**, *25*, 142–151. [CrossRef]
51. Mingsheng, P.; Mao, H.K.; Dien, L.; Mao, E.C.T. Raman Spectroscopy of Garnet-group Mineras. *Chin. J. Geochem.* **1994**, *13*, 176–183. [CrossRef]
52. Bersani, D.; Andò, S.; Vignola, P.; Moltifiori, G.; Marino, I.-G.; Lottici, P.-P.; Diella, V. Micro-Raman spectroscopy as a routine tool for garnet analysis. *Spectrochim. Acta* **2009**, *A73*, 484–491.
53. Salters, V.J.M.; Shimizu, N. World-Wide occurrence of HFSE-depleted mantle. *Geochim. Cosmochim. Acta* **1988**, *52*, 2177–2182. [CrossRef]
54. Huang, E.; Chen, C.H.; Huang, T.; Lin, E.H.; Xu, J.-A. Raman spectroscopic characteristics of Mg-Fe-Ca pyroxenes. *Am. Mineral.* **2000**, *85*, 473–479. [CrossRef]
55. D'Ippolito, V.; Andreozzi, G.B.; Bersani, D.; Lottici, P.-P. Raman fingerprint of chromate, aluminate andferrite spinels. *J. Raman Spectrosc.* **2015**. [CrossRef]
56. Bersani, D.; Aliatis, I.; Tribaudino, M.; Mantovani, L.; Benisek, A.; Carpenter, M.A.; Gatta, G.D.; Lottici, P.-P. Plagioclase composition by Raman spectroscopy. *J. Raman Spectrosc.* **2018**. [CrossRef]
57. Kloprogge, J.T. Chapter 6—Raman Spectroscopy of Clay Minerals. *Dev. Clay Sci.* **2017**, *8*, 150–199.
58. Hunter, R.H. Texture development in cumulate rocks. In *Layered Intrusions*; Cawthorn, R.G., Ed.; Elsevier: Amsterdam, The Netherland, 1996; pp. 77–102.
59. Lambart, S.; Laporte, D.; Schiano, P. Markers of the pyroxenite contribution in the major-element compositions of oceanic basalts: Review of the experimental constraints. *Lithos* **2013**, *160*, 14–36. [CrossRef]
60. Kempton, P.D.; Downes, H.; Sharkov, E.V.; Vetrin, V.R.; Ionov, D.A.; Carswell, D.A.; Beard, A. Petrology and geochemistry of xenoliths from the Northern Baltic shield: Evidence for partial melting and metasomatism in the lower crust beneath an Archean terrane. *Lithos* **1995**, *36*, 157–184. [CrossRef]
61. Gale, A.; Dalton, C.A.; Langmuir, C.H.; Su, Y.; Schilling, J.-G. The mean composition of ocean ridge basalts. *Geochem. Geophys. Geosyst.* **2013**, *14*. [CrossRef]
62. Zhong, Y.; Liu, W.; Sun, Z.; Yakymchuk, C.; Ren, K.; Liu, J.; Li, W.; Ma, Y.; Xia, B. Geochemistry and Mineralogy of Basalts from the South Mid-Atlantic Ridge (18.0°–20.6°S): Evidence of a Heterogeneous Mantle Source. *Minerals* **2019**, *9*, 659. [CrossRef]
63. Pearce, J.A. Geochemical fingerprint of oceanic basalts with applications to ophiolite classification and the search for Archean oceanic crust. *Lithos* **2008**, *100*, 14–48. [CrossRef]
64. Smith Nagihara, S.; Casey, J.F. Whole-Rock geochemistry of amphibolites and metagabbros from the West Iberia Margin, Leg 173. *Proc. Ocean. Drill. Prog. Sci. Results* **2001**, *173*, 1–20.
65. Grimes, C.B.; John, B.E.; Kelemen, P.B.; Mazdab, F.K.; Wooden, J.L.; Cheadle, M.J.; Hanghøj, K.; Schwartz, J.J. Trace element chemistry of zircons from oceanic crust: A method for distinguishing detrital zircon provenance. *Geology* **2007**, *35*, 643. [CrossRef]
66. Geisler, T.; Pidgeonm, R.T.; Van Bronswijkc, W.; Kurtza, R. Transport of uranium, thorium and lead in metamict zircon under low-temperature hydrothermal conditions. *Chem. Geol.* **2002**, *191*, 141–154. [CrossRef]
67. Bea, F.; Bortnikov, N.; Montero, P.; Zinger, T.; Sharkov, E.; Silantyev, S.; Skolotnev, S.; Trukhalev, A.; Francisco Molina-Palma, J. Zircon xenocryst evidence for crustal recycling at the Mid-Atlantic Ridge. *Lithos*, 2020; 355–361. [CrossRef]
68. Borisov, A.; Aranovich, L. Zircon solubility in silicate melts: New experiments and probability of zircon crystallization in deeply evolved basic melts. *Chem. Geol.* **2019**, *510*, 103–112. [CrossRef]
69. Nozaka, T.; Meyer, R.; Wintsch, R.P.; Wathen, B. Hydrothermal spinel, corundum and diaspore in lower oceanic crustal troctolites from the Hess Deep Rift. *Contrib. Mineral. Petrol.* **2016**, *171*, 53. [CrossRef]
70. Sanfilippo, A.; Dick, H.J.B.; Ohara, Y.; Tiepolo, M. New insights on the origin of troctolites from the breakaway area of the Godzilla Megamullion (Parece Vela back-arc basin): The role of melt-mantle interaction on the composition of the lower crust. *Isl. Arc* **2016**, *25*, 220–234. [CrossRef]
71. Leake, B.E.; Woolley, A.R.; Arps, C.E.S.; Birch, W.D.; Gilbert, M.C.; Grice, J.D.; Hawthorne, F.; Kato, A.; Kisch, H.J.; Krivovichev, V.G.; et al. Nomenclature of amphiboles: Report of the Subcommittee on Amphi-boles of the International Mineralogical Association, Commission on New Minerals and Mineral Names. *Am. Mineral.* **1997**, *82*, 1019–1037.

72. Dragovic, B.; Baxter, E.F.; Caddick, M.J. Pulsed dehydration and garnet growth during subduction revealed by zoned garnet geochronology and thermodynamic modeling, Sifnos, Greece. *Earth Planet. Sci. Lett.* **2015**, *413*, 111–122. [CrossRef]
73. Andrews, A.J.; Gardner, J.E.; Housh, T.B. Repeated recharge, assimilation and hybridization in magmas erupted from El Chichón as recorded by plagioclase and amphibole phenocrysts. *J. Volcanol. Geotherm.* **2008**, *175*, 415–426. [CrossRef]
74. De Angelis, S.H.; Larsen, J.; Cooms, M.; Dunn, A.; Hayden, L. Amphibole reaction rims as a record of pre-eruptive magmatic heating: An experimental approach. *Earth. Planet. Sci. Lett.* **2015**, *426*, 235–245. [CrossRef]
75. Rutherford, M.; Devine, J. Magmatic conditions and magma ascent as indicated by hornblende phase equilibria and reactions in the 1995–2002 Soufrière Hills magma. *J. Petrol.* **2003**, *44*, 1433–1454. [CrossRef]
76. Baxter, E.F.; Caddick, M.J. Garnet growth as a proxy for progressive subduction zone dehydration. *Geology* **1993**, *41*, 643–646. [CrossRef]
77. Plümper, O.; Piazolo, S.; Austrheim, H. Olivine Pseudomorphs after Serpentinized Orthopyroxene Record Transient Oceanic Lithospheric Mantle Dehydration (Leka Ophiolite Complex, Norway). *J. Petrol.* **2012**, *53*, 1943–1968. [CrossRef]
78. Silantyev, S.A. Origin Conditions of the Mid-Atlantic Ridge Plutonic Complex at 13°–17° N. *Petrology* **1998**, *6*, 351–387.
79. Johnson, M.C.; Rutherford, M.J. Experimental calibration of the aluminum-in-hornblende geobarometer with application to Long Valley caldera (California) volcanic rocks. *Geology* **1989**, *17*, 837–841. [CrossRef]
80. Wolf, M.B.; Wyllie, P.J. Garnet growth during amphibolite anatexis—Implications of a garnetiferous restite. *J. Geol.* **1993**, *101*, 357–373. [CrossRef]
81. Léger, A.; Ferry, J.M. Highly aluminous hornblende from low-pressure metacarbonates and a preliminary thermodynamic model for the Al content of calcic amphibole. *Am. Mineral.* **1991**, *76*, 1002–1017.
82. Berger, J.; Féménias, O.; Mercier, J.-C.C. Ocean-Floor hydrothermal metamorphism in the Limousin ophiolites (western French Massif Central): Evidence of a rare preserved Variscan oceanic marker. *J. Metamorph. Geol.* **2005**, *23*, 795–812. [CrossRef]
83. Newton, R.C.; Manning, C.E. Solubility of corundum in the system Al_2O_3–SiO_2–H_2O–NaCl at 800 °C and 10 kbar. *Chem. Geol.* **2008**, *249*, 250–261. [CrossRef]
84. Salvi, S.; Williams-Jones, A.E. The role of hydrothermal processes in concentrating high-field strenght elements in the Strange Lake peralkaline complex, northeastern Canada. *Geochim. Cosmochim. Acta* **1996**, *60*, 1917–1932. [CrossRef]
85. Hoskin, P.W.O.; Kinny, P.D.; Wyborn, D. Chemistry of hydrothermal zircon: Investigating timing and nature of water-rock interaction. *Water Rock Interact.* **1998**, *9*, 545–548.
86. Aarnes, I.; Svensen, H.; Connolly, J.A.D.; Podladchikov, Y.Y. How contact metamorphism can trigger global climate changes: Modeling gas generation around igneous sills in sedimentary basins. *Geochim. Cosmochim. Acta* **2010**, *74*, 7179–7195. [CrossRef]
87. Leeman, V.P.; Annen, C.; Dufek, J. Snaker River Plain—Yellowstone silicic volcanism: Implications for magma genesis and magma fluxes. *Geol. Soc. Spec. Publ.* **2008**, *304*, 235–258. [CrossRef]
88. Almeev, R.R.; Holtz, F.; Koepke, J.; Parat, F. Experimental calibration of the effect of H_2O on plagioclase crystallization in basaltic melt. *Am. Mineral.* **2012**, *97*, 1234–1240. [CrossRef]
89. Schmincke, H.-U. *Volcanism*; Springer: Berlin/Heidelberg, Germany, 1988; p. 324.
90. Shaw, C.S.J.; Klügel, A. The pressure and temperature conditions and timing of glass formation in mantle-derived xenoliths from Baarley, West Eifel, Germany: The case for amphibole breakdown, lava infiltration and mineral–melt reaction. *Mineral. Petrol.* **2002**, *74*, 163–187. [CrossRef]
91. Sapienza, G.; Griffin, W.L.; O'Reilly, S.Y.; Morten, L. Petrology and Sr–Nd–Hf isotope geochemistry of gabbro xenoliths from the Hyblean Plateau: A MARID reservoir beneath SE Sicily? *Contrib. Mineral. Petrol.* **2009**, *157*, 1–22. [CrossRef]
92. Cannata, A.; Scribano, V. Specific gravity measures on deep-seated nodules from Sicily. *Rend. Soc. Geol. Ital.* **1990**, *13*, 97–98.
93. Punturo, R.; Kern, H.; Scribano, V.; Atzori, P. Petrophysical and petrological characteristics of deep-seated xenoliths from Hyblean Plateau, south-eastern Sicily, Italy: Suggestions for a lithospheric model. *Mineral. Petrogr. Acta* **2000**, *43*, 1–20.

94. Christensen, N.I. Elasticity of ultrabasic rocks. *J. Geophys. Res.* **1966**, *71*, 5921–5931. [CrossRef]
95. Miller, D.J.; Christensen, N.I. Seismic velocities of lower crustal and upper mantle rocks from the slow spreading Mid-Atlantic Ridge, south of the Kane Transform zone (MARK). *Proc. Ocean. Drill. Program. Part B Sci. Results* **1997**, *153*, 437–454.
96. Jull, M.; Kelemen, P.B. On the conditions for low Experimental calibration of the aluminum-in-hornblende geobarometer with application to Long Valley caldera (California) volcanic rocks and crustal convective instability. *J. Geophys. Res.-Solid* **2001**, *106*, 6423–6446. [CrossRef]
97. Bunge, H.P.; Richards, M.A.; Baumgardner, J.R. A sensitivity study of three-dimensional spherical mantle convection at 108 Rayleigh number: Effects of depth-dependent viscosity, heating mode and endothermic phase change. *J. Geophys. Res. Solid Earth* **1997**, *102*, 11991–12007. [CrossRef]
98. Houseman, G.A.; Molnar, P. Gravitational (Rayleigh-Taylor) instability of a layer with non-linear viscosity and convective thinning of continental lithosphere. *Geophys. J. Int.* **1997**, *128*, 125–150. [CrossRef]
99. Rayleigh, L. Investigation of the character of an incompressible heavy fluid of variable density. *Proc. Lond. Math. Soc. J.* **1997**, *1*, 170–197. [CrossRef]
100. Taylor, G.I. The instability of liquid surfaces when accelerated in a direction perpendicular to their planes. *Proc. R. Soc. Lond. Set.* **1950**, *201*, 192–196.
101. Brueckner, H.K. Sinking intrusion model for the emplacement of garnet-bearing peridotites into continent collision orogens. *Geology* **1998**, *26*, 631–634. [CrossRef]
102. Mével, C. Serpentinization of abyssal peridotites at mid-ocean ridges. *C. R. Geosci.* **2003**, *335*, 825–852. [CrossRef]
103. Snow, J.E.; Edmond, H.N. Ultraslow-Spreading ridges rapid paradigm changes. *Oceanography* **2007**, *20*, 90–101. [CrossRef]
104. Cannat, M.; Sauter, D.; Lavier, L.; Bickert, M.; Momoh, E.; Leroy, S. On spreading modes and magma supply at slow and ultraslow mid-ocean ridges. *Earth Planet. Sci. Lett.* **2019**, *519*, 223–233. [CrossRef]
105. Qin, Y.; Singh, S.C. Seismic evidence of a two-layer lithospheric deformation in the Indian Ocean. *Nat. Commun.* **2015**, *6*, 1–11. [CrossRef] [PubMed]
106. Hirth, G.; Kohlstedt, D.L. Water in the oceanic upper mantle; implications for rheology, melt extraction and the evolution of the lithosphere. *Earth Planet. Sci. Lett.* **1996**, *144*, 93–108. [CrossRef]
107. Fryer, P. Recent Studies of Serpentinite Occurrences in the Oceans: Mantle-Ocean Interactions in the Plate Tectonic Cycle. *Geochemistry* **2002**, *62*, 257–302. [CrossRef]
108. Christensen, N.I. The Abundance of Serpentinites in the Oceanic Crust. *J. Geol.* **1972**, *80*, 709–719. [CrossRef]
109. Ramberg, H. Model Experimentation of the Effect of Gravity on Tectonic Processes. *Geophys. J. R. Astr. Soc.* **1967**, *14*, 307–329. [CrossRef]
110. Tikoff, B.; Wojtal, F. Displacement control of geological structures. *J. Struct. Geol.* **1999**, *21*, 959–967. [CrossRef]
111. Lobkovsky, L.I.; Ismail-Zadeh, A.T.; Krasovsky, S.S.; Kuprienko, P.Y.; Cloetingh, S. Gravity anomalies and possible formation mechanism of the Dnieper–Donets Basin. *Tectonophysics* **1996**, *268*, 281–292. [CrossRef]
112. Zhu, W.; Wong, T.-F. Network modeling of the evolution of permeability and dilatancy in compact rock. *J. Geophys. Res.* **1999**, *104*, 2963–2971. [CrossRef]
113. Handy, M.R. The solid-state flow of polymineralic rocks. *J. Geophys. Res.* **1990**, *95*, 8647–8661. [CrossRef]
114. Coleman, R.G. Plate tectonic emplacement of Upper mantle peridotites along continental edges. *J. Geophys. Res.* **1971**, *76*, 1212–1222. [CrossRef]
115. Francis, T.J.G. Serpentinization faults and their role on the tectonics of slow-spreading ridges. *J. Geophys. Res.* **1981**, *86*, 11616–11622. [CrossRef]
116. Ismail-Zadeh, A.T.; Panza, G.F.; Naimark, B.M. Stress in the Descending Relic Slab beneath Vrancea Region, Romania. *Pure Appl. Geophys.* **2000**, *157*, 111–130. [CrossRef]
117. Fuchs, K.; Bonjer, K.-P.; Bock, G.; Cornea, I.; Radu, C.; Enescu, D.; Jianu, D.; Nourescu, A.; Merkler, G.; Moldoveanu, T.; et al. The Romanian Earthquake of March 4, 1977. II. Aftershocks and Migration of Seismic Activity. *Tectonophysics* **1979**, *53*, 225–247. [CrossRef]
118. Saccani, E. A new method of discriminating different types of post-Archean ophiolitic basalts and their tectonic significance using Th-Nb and Ce-Dy-Yb systematics. *Geosci. Front.* **2015**, *6*, 481–501. [CrossRef]
119. Hirschmann, M.M.; Stolper, E.M. A possible role for garnet pyroxenite in the origin of the garnet signature in MORB. *Contrib. Mineral. Petrol.* **1996**, *124*, 185–208. [CrossRef]

120. Hirschmann, M.M.; Kogiso, T.; Baker, M.B.; Stolper, E.M. Alkalic magmas generated by partial melting of garnet pyroxenite. *Geology* **2003**, *31*, 481–484. [CrossRef]
121. Maffione, M.; Thieulot, C.; van Hinsbergen, D.J.J.; Morris, A.; Plümper, O.; Spakman, W. Dynamics of intraoceanic subduction initiation: 1. Oceanic detachment fault inversion and the formation of supra-subduction zone ophiolites. *Geochem. Geophys. Geosyst.* **2015**, *16*. [CrossRef]
122. Palin, R.M.; Santosh, M.; Cao, W.; Li, S.S.; Hernández-Uribe, D.; Parsons, A. Secular change and the onset of plate tectonics on Earth. *Earth-Sci. Rev.* **2020**. [CrossRef]